

# High $Q^2$ $\pi^0$ electroproduction in the resonance region

M. Ungaro, K. Joo

November 17, 2023

## Abstract

We report the analysis of exclusive single  $\pi^0$  electroproduction in the resonance region at Jefferson Lab in the  $Q^2$  range  $2 \rightarrow 6$  GeV $^2$ .  $\pi^0$  c.m. angular distributions are obtained over the entire  $4\pi$  c.m. solid angle. The c.m. differential cross sections and beam spin asymmetries are measured.

## Contents

<b>1 Electron identification</b>	<b>3</b>
1.1 CC theta Matching . . . . .	4
1.2 CC phi Matching . . . . .	7
1.3 CC time Matching . . . . .	8
1.4 EC Threshold . . . . .	10
1.5 EC Sampling Fraction . . . . .	10
1.5.1 Cut parameters . . . . .	14
1.6 Track Coordinates in the EC plane . . . . .	15
1.7 Minimum Ionizing Particles (MIP) rejection . . . . .	20
1.8 Electromagnetic Shower Shape . . . . .	22
1.9 Number of photo-electrons in the Čerenkov detector . . . . .	22
1.10 Summary of Electron Identification . . . . .	25
<b>2 Proton identification</b>	<b>26</b>
2.1 CLAS Timing . . . . .	26
2.2 $\Delta T$ cut . . . . .	26
2.2.1 Cut parameters . . . . .	27
<b>3 Vertex Correction, Selection</b>	<b>31</b>
3.1 Beam Offset . . . . .	31
3.2 Vertex Correction, Cut . . . . .	32
<b>4 Fiducial Cuts</b>	<b>35</b>
4.1 Introduction . . . . .	35
4.2 Traditional cuts on the electron lab coordinates $\phi, \theta, p$ . . . . .	35
4.3 $\theta$ versus momentum cuts . . . . .	38
4.4 Cuts on detectors coordinates . . . . .	38
4.4.1 Detectors inefficiencies . . . . .	41
4.4.2 Comparison with the traditional cuts . . . . .	41

<b>5</b>	<b>Electron Kinematic Correction</b>	<b>45</b>
5.1	Introduction . . . . .	45
5.2	Correction effects on the elastic peak . . . . .	45
5.3	Correction effects on the $eP(\pi^0)$ missing mass . . . . .	48
5.4	Correction effects on the $eP(\eta)$ missing mass . . . . .	50
APPENDICES		
.1	Fiducial cut tent function . . . . .	53
.2	Fiducial cut tent function . . . . .	54
.3	Momentum Correction Parameters and function . . . . .	55

## 1 Electron identification

In CLAS electro-production experiments the scattered electron defines the timing of each event, so it is particularly important to make sure that their identification is correct and that there is no contamination from particles such as  $\pi^-$ .

We consider candidate electrons every negative track that produced a hardware trigger (this trigger condition is ensured by choosing the first entry in the EVNT bank). The track is also required to have hit matches in the CLAS Čerenkov (CC)[\[7\]](#), Drift Chambers (DC)[\[4\]](#), Electromagnetic Calorimeter (EC)[\[6\]](#) and Time of Flight (SC or TOF)[\[11\]](#), and to have time-based reconstruction (positive DC status word in DCPB).

Starting from a candidate electron, we use the following studies, detailed in the following sections, to defined good electron:

- CC  $\theta$ ,  $\phi$  and time matching in the detector
- EC Threshold
- EC Sampling Fraction
- Track Coordinates in the EC plane
- Minimum Ionizing Particles rejection in the EC
- Electromagnetic Shower Shape in the EC
- Number of photo-electrons ( $nphe$ ) in the CC This cut is not used anymore for identification, but the distributions will be shown for comparison with other analyses of e16 data

For each individual cut we will show four histograms to illustrate its impact:

- a. Variable distribution when no cut at all is applied.
- b. Variable distribution when all other pid cuts but this one are applied: this helps refining cut parameters. For example, when looking at the sampling fraction, applying all other cuts to helps clean up the plot and to better estimate the sampling fraction cut. We also refer as “calorimeter cuts” all cuts but the  $nphe$  and EC threshold.
- c. Variable distribution all the pid cuts are reversed: these should be particles other than electrons. This condition can help identifying possible contamination.
- d. Variable distribution when all cuts, including the one under study, are applied.

The statistics and effectiveness of each case is reported in the plots. Only the relevant plots are reported here. The complete set of plots can be found on the web [\[10\]](#).

## 1.1 CC theta Matching

This, and the following CC  $\phi$  and Time Matching procedures, are based on a study [9, 3, 2] of the Čerenkov response function.

The CC  $\theta$  matching requires the candidate electrons tracks to match a signal in the CC. The CC segments (one pmt from the right and the corresponding from the left, constitute a segment) and mirrors are placed along the CLAS polar angle. Since the torus magnetic field bend the electrons toward the beamline, it's convenient not to use the track  $\theta$  angle at the vertex but the angle  $\theta_{CC}$  of the point of intersection of the track with the CC plane. These are the details of the  $\theta_{CC}$  calculation:

1. The intersection of the track with the TOF plane  $\vec{P}_0$  is considered (DCPB bank).
2. The normalized direction of the track  $\vec{n}$  of the track to the TOF plane is considered (DCPB bank).
3. The line representing the un-bending track is then  $\vec{P} = \vec{P}_0 - t\vec{n}$  (the minus sign accounts for the fact that the CC is before the TOF).
4. The CC plane equation is considered:  $Ax + By + Cz + D = 0$ , with  $A = -0.000784$ ,  $B = 0$ ,  $C = -0.00168$ , and  $D = 1$  [9]. This is also represented by the vector  $\vec{S} = (A, B, C)$
5. Substituting the line equation in the plane equation one finds the distance of the path length from the intersection of the track with the TOF plane and the intersection of the track with the CC plane:

$$t = \frac{\vec{S} \cdot \vec{P}_0}{\vec{S} \cdot \vec{n}}$$

There should be one to one correspondence between  $\theta_{CC}$  and segment number for real tracks, while background noise and accidentals should show no such correlation. For each segment, the  $\theta_{CC}$  distribution is fitted with a gaussian + second order polynomial distribution to determine its mean and width. Examples of these fits can be found in Fig. 1. Events that have  $\mu - 4\sigma < \theta_{CC} < \mu - 3\sigma$  pass the cut (this accounts for the distribution not being completely symmetric around the mean). The overall  $\theta_{CC}$  versus segment distribution and the lower/upper limits are shown in Fig. 2.

There are two exception to this cut:

1. The first and last segments distributions is hard to fit. The cut in this case is ignored.
2. If both (left and right) photomultiplier have a signal the track is kept.

The events that fall in this category can be seen in the bottom right panel in Fig. 2.

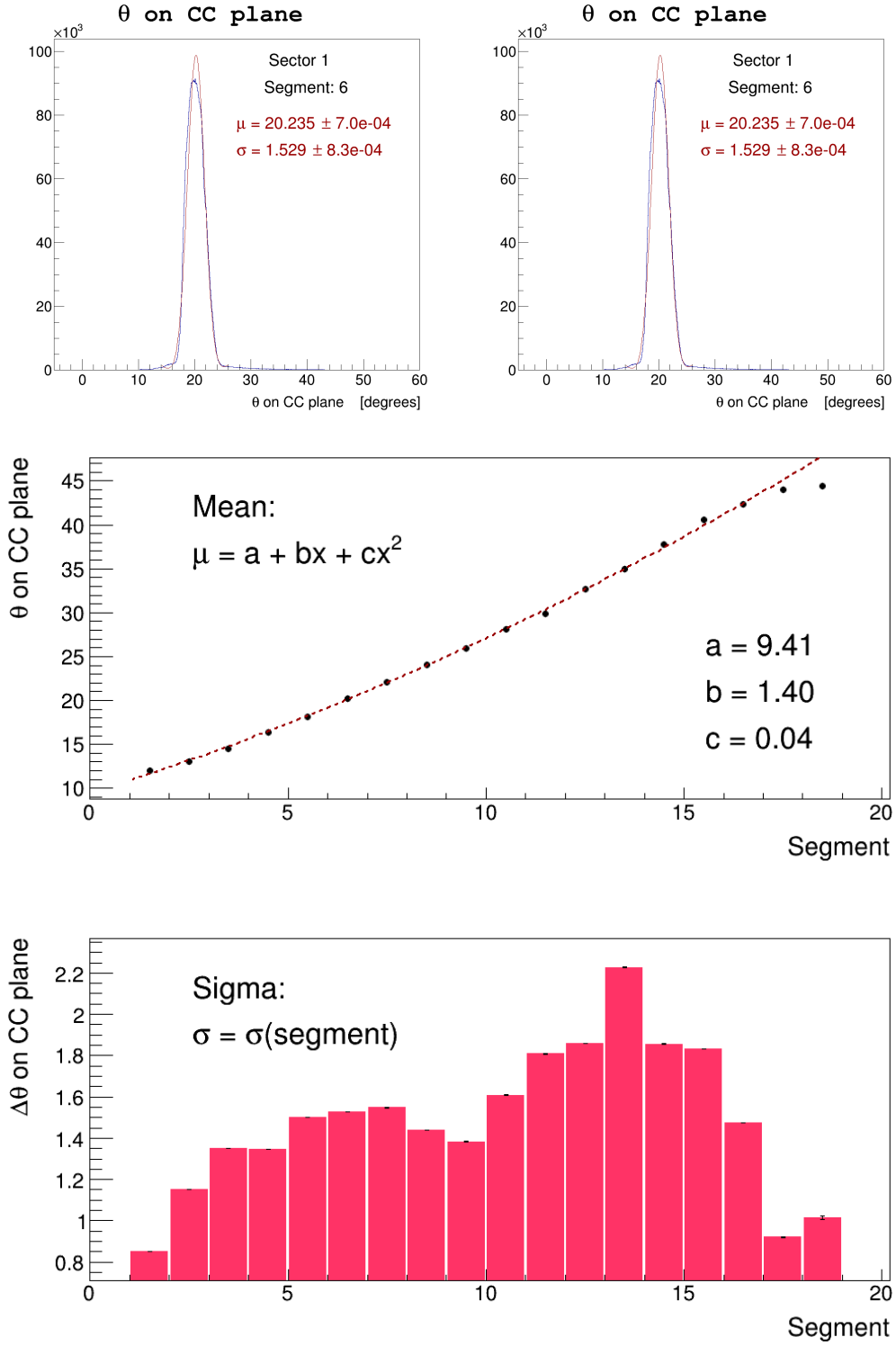


Figure 1: Top panels:  $\theta_{CC}$  for two segments in sector 1, and gaussian + second order polynomial fit. The distribution is slightly asymmetric to the left, so the lower limit was  $4\sigma$  while the upper limit was  $3\sigma$ . Bottom Panels: the mean distribution is fitted with a third order polynomial.

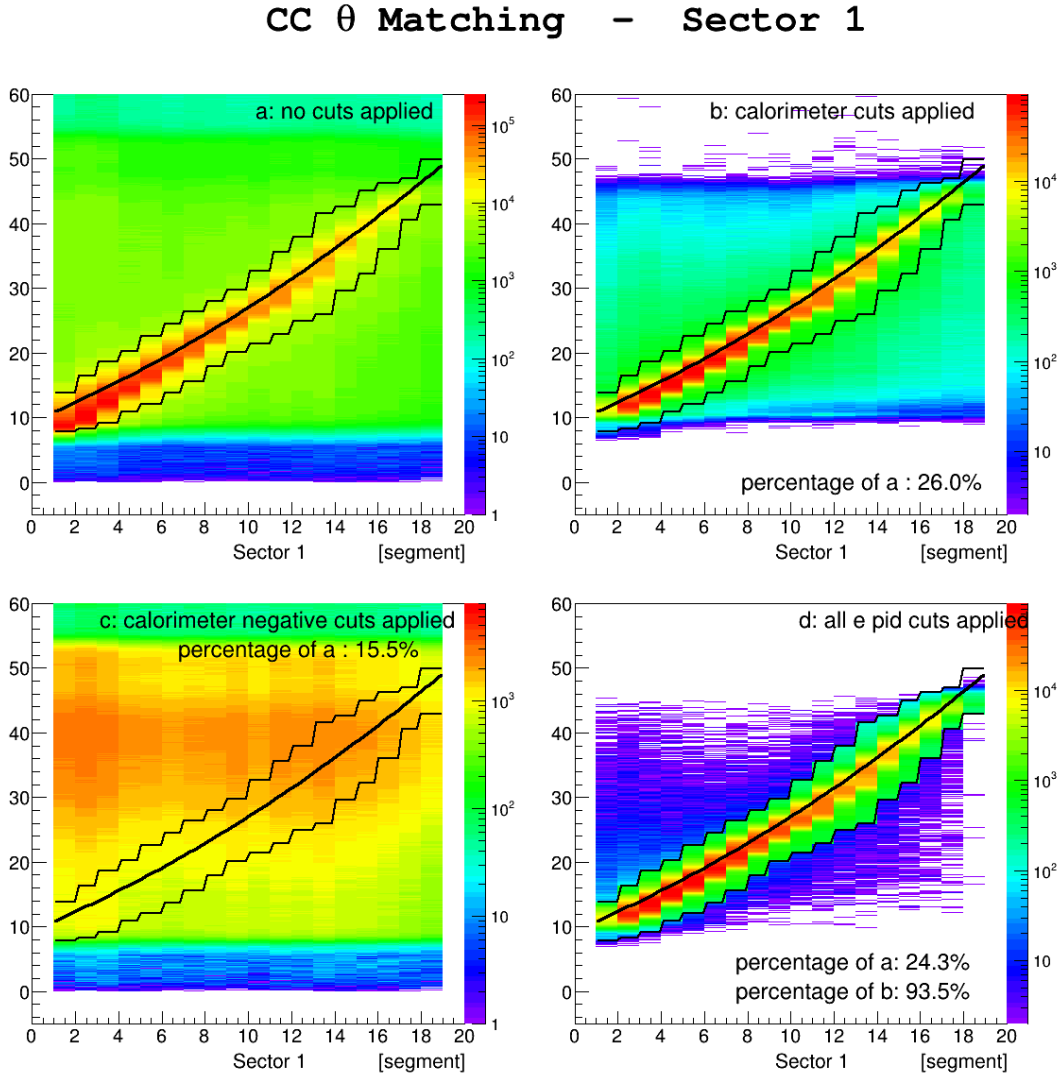


Figure 2:  $\theta_{CC}$  versus Segment for Sector 1. The  $\theta_{CC}$  distribution for each segment is fitted with a gaussian + second order polynomial distribution to determine its mean and width. Events that have  $\mu - 4\sigma < \theta_{CC} < \mu - 3\sigma$  pass the cut. Top left: all events. Top right: events with calorimeter cuts applied (notice that these cuts remove 74 % of the data). Bottom left: events with the negative calorimeter cuts applied. Bottom right: all cuts applied. Notice that the CC matching cut only removes 7 % of the events with the calorimeter cuts already applied.

## 1.2 CC phi Matching

The principle of this cut is very simple: when the track is on the right of the CC, the right photo-multiplier should fire, and vice-versa. Exception: when  $\phi$  (relative to the center in each sector) is less than  $4^0$  the track is kept (the Čerenkov light should hit both pmts, but with less efficiency since it splits in the middle) [9, 3, 2].

To show the effects of this cut the quantity “ $\phi$  matching” is plotted in Fig. 3. This quantity is 0 when both pmts are fired, 1(−1) when there is a left (right) match and 2(−2) there is a left (right) mismatch. The cut applied is: “ $\phi$  matching” < 2 except when  $|\phi| < 4^0$ .

<b>φ matching cut:</b>	→ no cuts applied	0: both pmts fired
	→ calorimeters cuts applied	-1, 1: track/pmt same side
match  < 2    φ > 4	→ all cuts applied	-2, 2: track/pmt opposite side

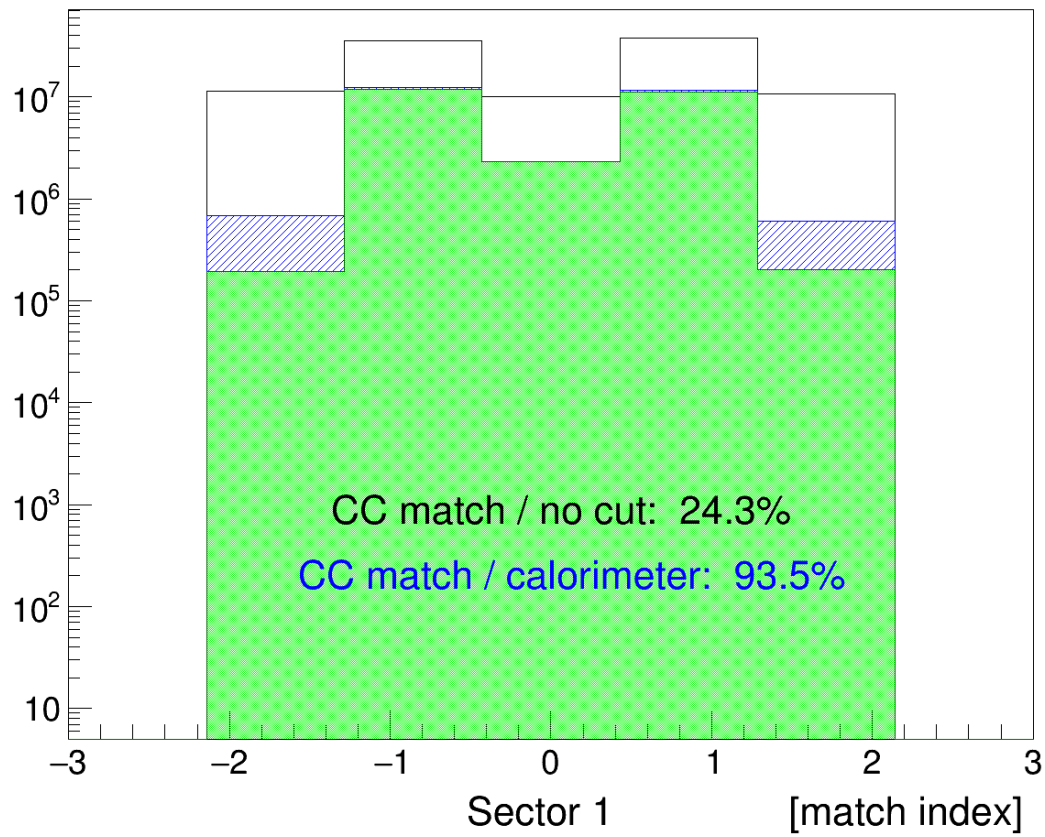


Figure 3: “ $\phi$  matching”: this quantity is 0 when both pmts are fired, 1(−1) when there is a left (right) match and 2(−2) there is a left (right) mismatch. The cut applied is: “ $\phi$  matching” < 2 except when  $|\phi| < 4^0$ .

### 1.3 CC time Matching

The CC timing was not calibrated in e1-6, but a timing cut is still possible if applied to each tube (this is basically equivalent to perform the timing calibration).

The difference  $\Delta T$  between the track time recorded on a CC segment and corresponding time recorded on the TOF, corrected for the path length from the CC to the TOF, is fitted with a gaussian (see Fig. 4). Since there could be multiple Čerenkov light reflections leading to a time delay, a 3 sigma cut is applied on the *left* of the signal, and not on the right. This difference is plotted in Fig. 5 for all tubes in sector one.

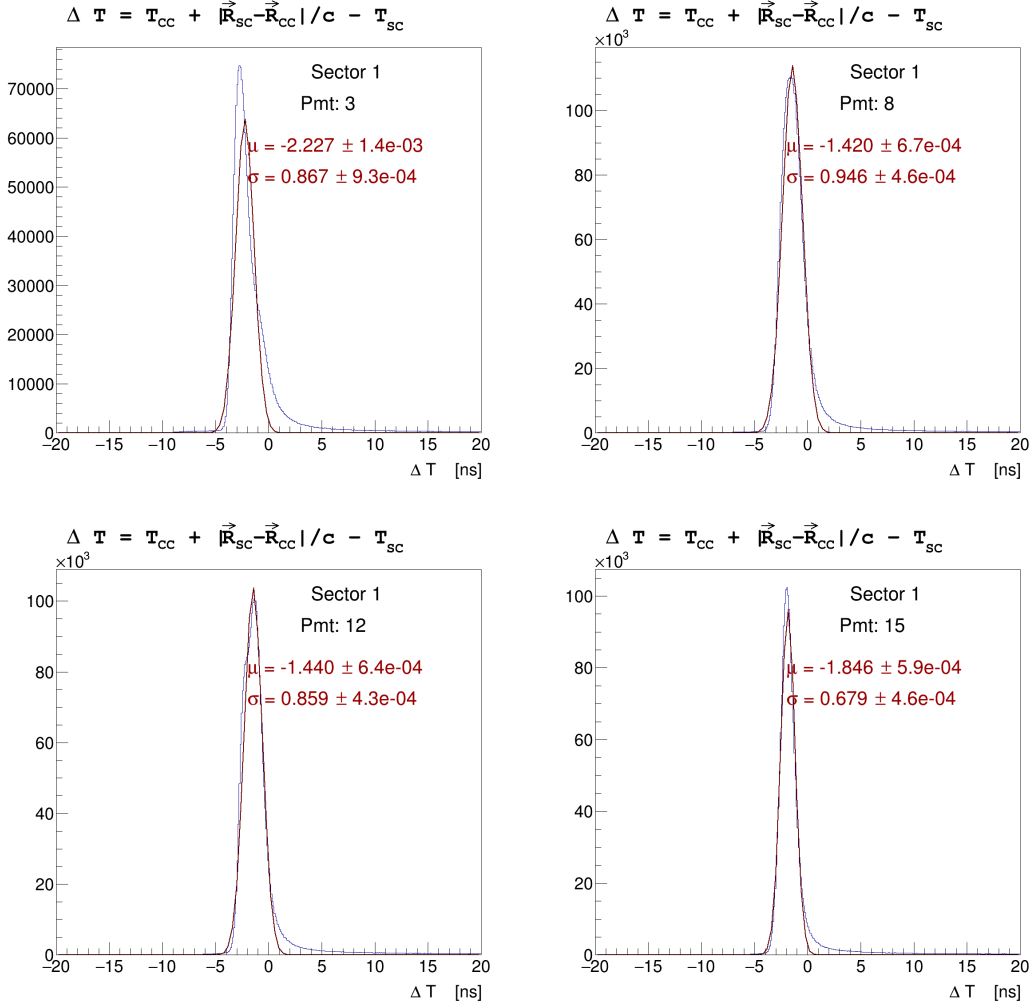


Figure 4: CC time matching. The difference  $\Delta T$  between the track time recorded at a CC tube ( $T_{CC}$ ) and corresponding time recorded on the TOF ( $T_{SC}$ ), corrected for the path length from the CC to the TOF ( $|R_{CC} - R_{SC}|/c$ ), shown here for 4 CC pmts, is fitted with a gaussian. A  $5\sigma$  cut is applied on the left of the signal.

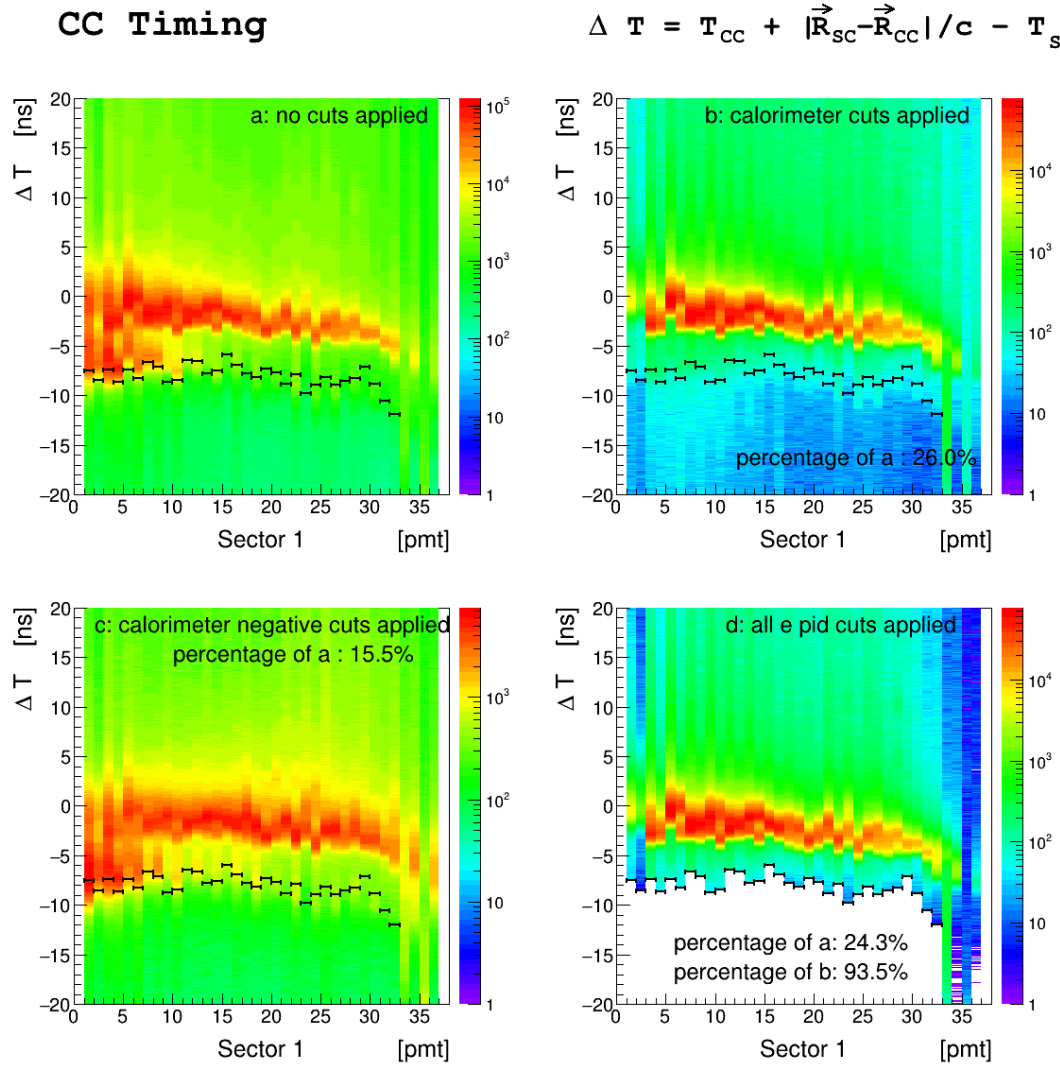


Figure 5: CC time matching. The difference  $\Delta T$  between the track time recorded at a CC tube ( $T_{CC}$ ) and corresponding time recorded on the TOF ( $T_{SC}$ ), corrected for the path length from the CC to the TOF ( $|\vec{R}_{CC} - \vec{R}_{SC}|/c$ ), is fitted with a gaussian. A  $3\sigma$  cut is applied on the left of the signal. Top left: all events. Top right: events with calorimeter cuts applied. notice that these cuts remove 71 % of the data. Bottom left: events with the negative calorimeter cuts applied. Bottom right: all cuts applied. Notice that the CC matching cut only removes 7 % of the events with the calorimeter cuts already applied.

## 1.4 EC Threshold

A study [8] of the inclusive cross section at various beam energies in CLAS results in a parametrization of the low momentum cut  $p_{min}$  as a function of the calorimeter low total threshold (in milliVolts) of the trigger discriminator:

$$p_{min} (\text{MeV}) = 214 + 2.47 \times EC_{threshold}(\text{mV}) \quad (1)$$

The low total threshold for e1-6 was 172 mV therefore the minimum momentum cut is fixed at:

$$p_{min} = 0.64 \text{ GeV}$$

Fig. 6 shows for the momentum distribution of the candidates integrated over all sectors. In average,  $\sim 27.7\%$  pass the all other particle ID cuts and of these,  $91.9\%$  pass the minimum  $p$  cut.

The cut value used is the same for all sectors and its effectiveness is summarized in table ??.

Sector	all other cuts GeV	minimum $p$ cut %
1	71.1	93.1
2	72.1	89.8
3	71.9	91.6
4	71.8	93.7
5	75.2	90.0
6	72.6	92.8

Table 1: The minimum  $p$  cut values and effectiveness in each sector. The last column refers to events with signal in EC that pass the minimum  $p$  cut.

## 1.5 EC Sampling Fraction

When going through the EC calorimeter, in the momentum range of particles detected in CLAS, charged pions are minimum ionizing particles, while electrons shower with a total energy deposition  $E_{tot}$  proportional to their momentum  $p$ . Therefore the sampling fraction  $E_{tot}/p$  should be independent of momentum (in reality there is a slight dependence).

The total energy in the calorimeter  $E_{tot}$  is not always calculated to be the sum of the energies in the inner and outer part of the calorimeter  $E_{in}$  and  $E_{out}$ , due to wrong calculation/comparison with the DC momentum [1]. In this analysis we recalculated  $E_{tot}$  as  $E_{in} + E_{out}$  when that happened, by taking the larger between  $E_{tot}$  and  $E_{in} + E_{out}$ .

After applying all the other electron ID cuts, the sampling fraction is plotted in each sector as a function of momentum (see Fig. 7). The plot is divided in 15 momentum slices and each slice is fitted with a gaussian + second order polynomial function. The final result is a 3rd order polynomial function that parametrizes the mean and the sigma of the sampling fraction as a function of  $p$ . Since the negative pions in this plot would be below the electrons, the cut chosen is not exactly symmetric around the mean, but looser on the upper part: upper:  $3.4\sigma$ ; lower:  $3\sigma$ .

In Fig. 8 the Sampling Fraction for sector 1 is plotted for no cuts, all other cuts, all other negative cuts and all cuts respectively. One can see that all the other cuts result in a quite good selection already, and that the sampling fraction cut (d) keeps  $\sim 90\%$  of those events.

In Fig. 9 a comparison of the sampling fraction in all sectors is shown. The cut values used in each sector and their effectiveness are summarized in table ???. The parameters used are listed in sec.1.5.1.

Sector	events with EC GeV	SF cut %	%
1	73.8	60.1	
2	74.7	59.0	
3	75.6	57.5	
4	73.0	58.5	
5	74.9	60.3	
6	75.0	58.5	

Table 2: The Sampling Fraction (SF) cut values and effectiveness in each sector. The second column refers to events with signal in EC that pass the SF cut.

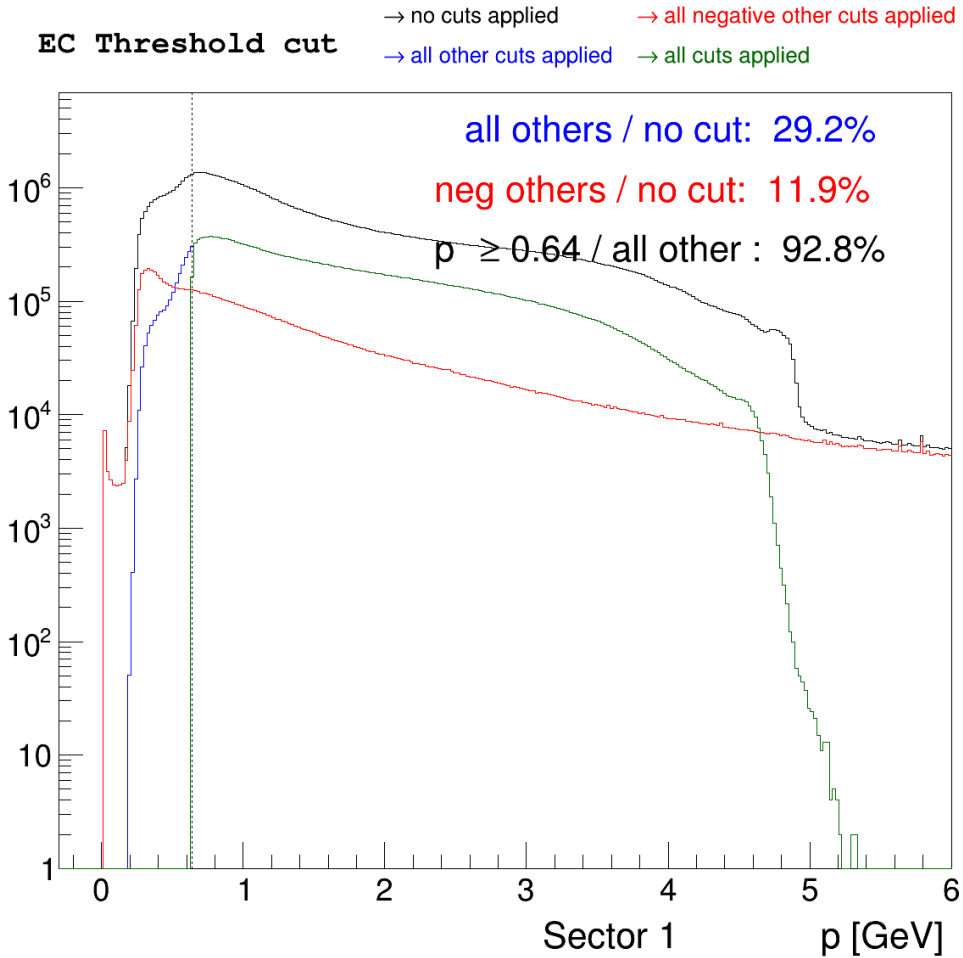


Figure 6: Candidates Momentum distribution in each sector. The minimum momentum cut is chosen according to Eq.1. In average,  $\sim 82\%$  of the candidates have a signal in the EC. Of those, 30 % pass the all other particle ID cuts and of these, 92.5 % pass the minimum  $p$  cut.

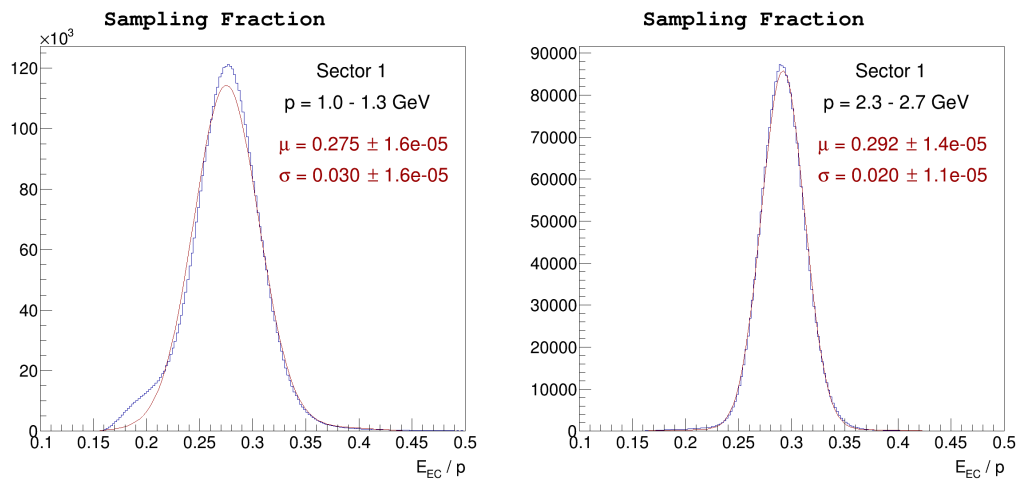
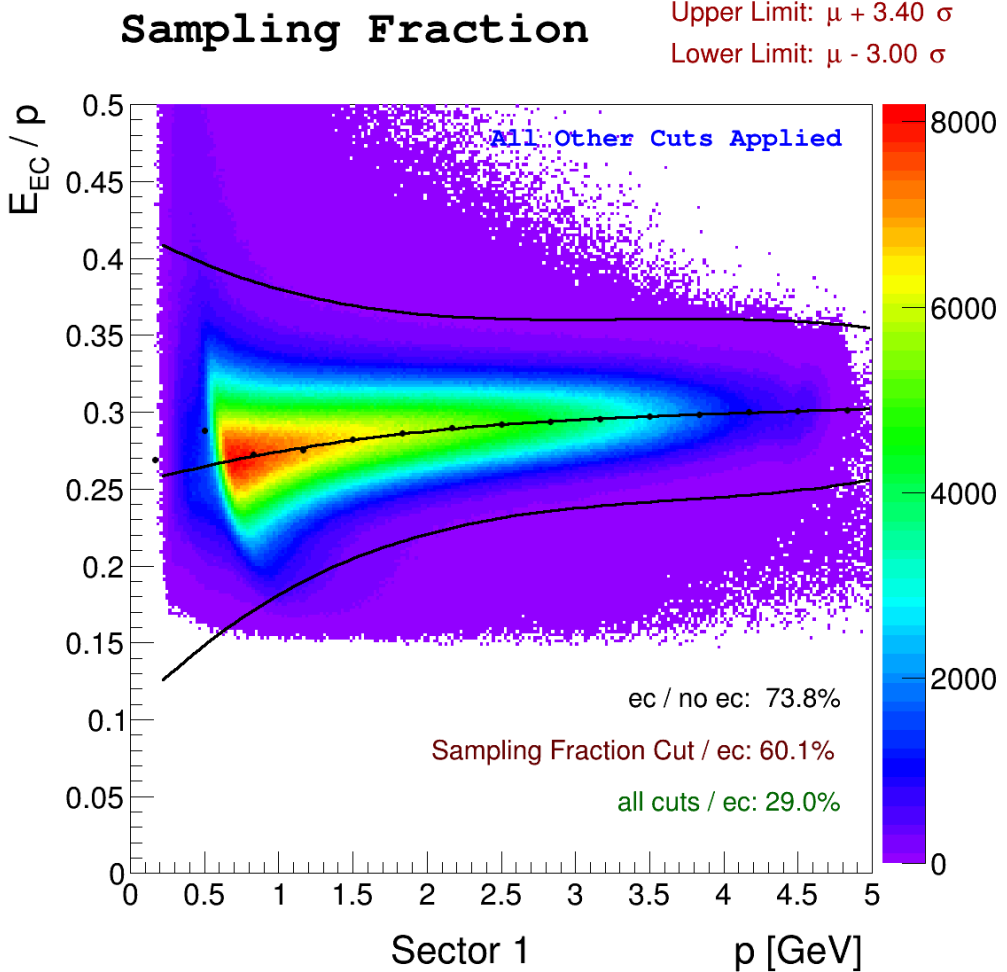


Figure 7: Top: Sampling Fraction as a function of momentum for sector 1. Bottom: four momentum slices, and gaussian + second order polynomial fit. The number of sigmas that define the cut are: upper:  $3.4\sigma$ ; lower:  $3\sigma$ .

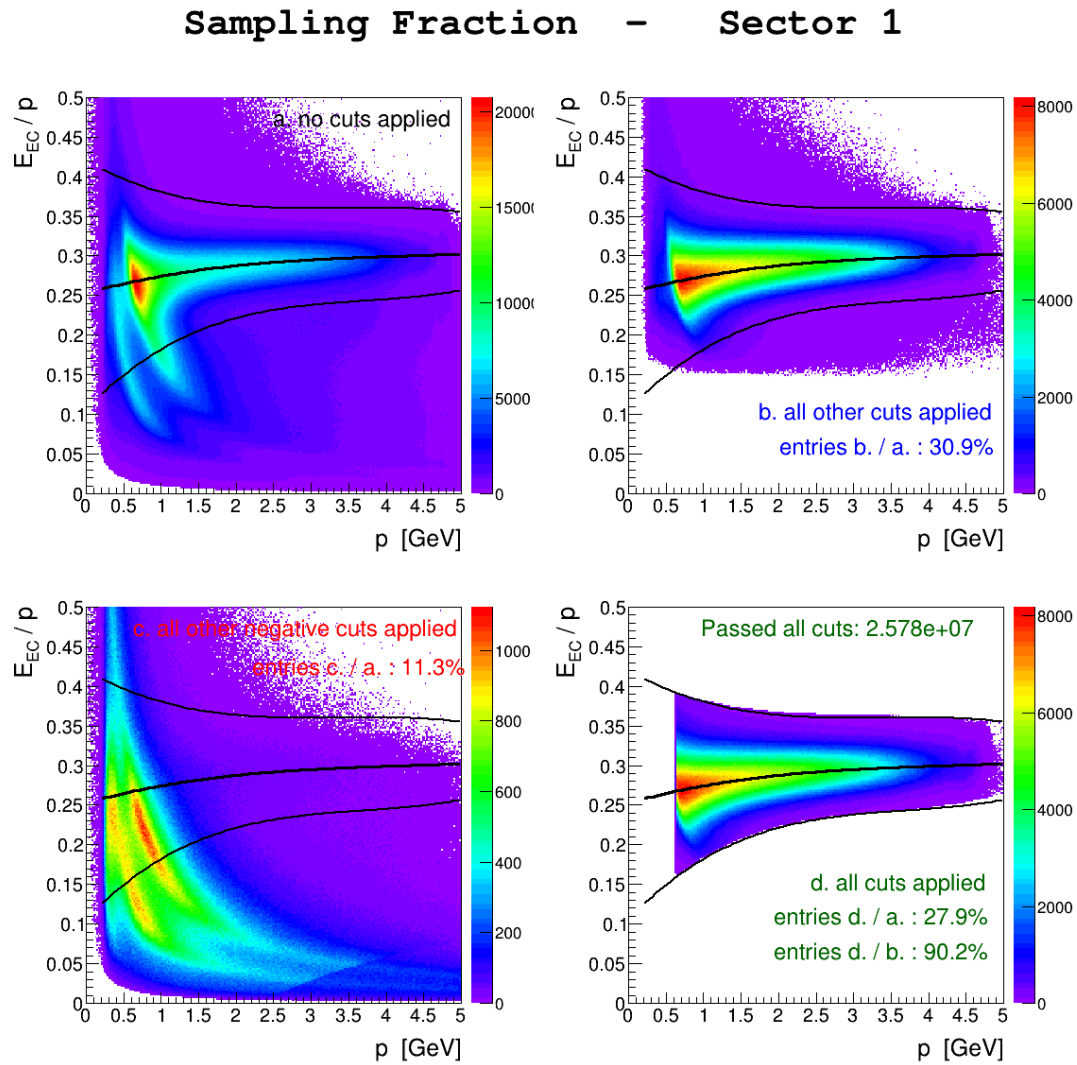


Figure 8: Sampling Fraction cut. Notice in panel (b) all the other cuts but the sampling fraction applied; the sampling fraction cut (d) keeps 90.5 % of the events in panel (b).

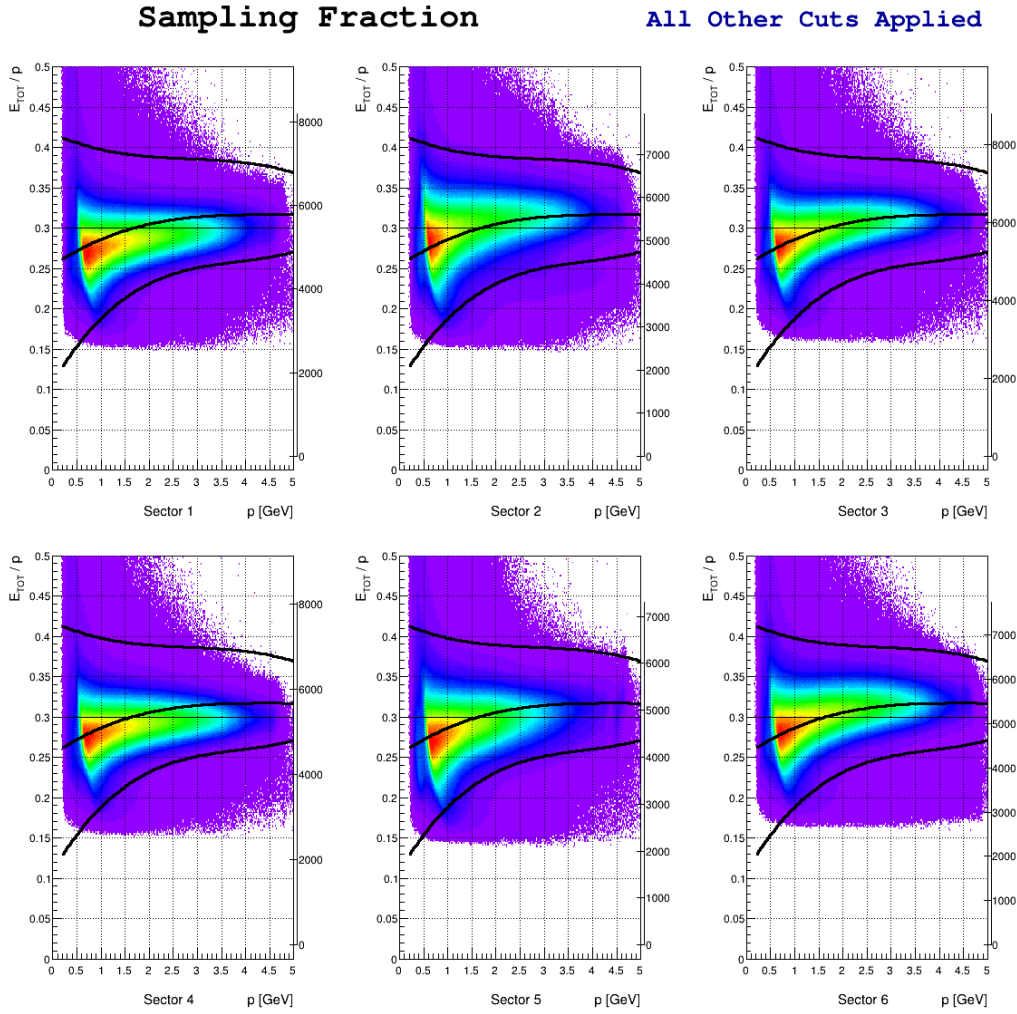


Figure 9: Sampling Fraction cut in all sectors. Plot grid and the line at 0.3 emphasize differences between sectors.

### 1.5.1 Cut parameters

$$f(p) = a + bp + cp^2 + dp^3$$

	S1	S2	S3	S4	S5	S6
<b>mean:</b>						
a:	0.249471	0.252591	0.250881	0.246831	0.247017	0.248919
b:	0.0350377	0.0487858	0.0443294	0.0381502	0.0326401	0.0467523
c:	-0.00887004	-0.0130587	-0.0101895	-0.00993875	-0.00788004	-0.0110489
d:	0.000827307	0.00120111	0.000785888	0.000882525	0.000684981	0.000902679
<b>sigma</b>						
a:	0.0482422	0.0501838	0.0483883	0.0435729	0.0463011	0.0452695
b:	-0.0234008	-0.0206365	-0.0243889	-0.018439	-0.0173496	-0.0180503
c:	0.00652057	0.00521743	0.00709145	0.00486129	0.00460028	0.00473553
d:	-0.000643782	-0.000504944	-0.000731488	-0.000498339	-0.00041353	-0.000477848

## 1.6 Track Coordinates in the EC plane

The EC is designed for the electron to release all their energy in it. However electrons that shower near the edges of the calorimeter will not loose all their energy in the detector because the shower is not fully contained, thus their energy cannot be properly reconstructed. For this reason, a fiducial cut is introduced on the track coordinates  $U, V, W$  of the electrons at the EC plane. The  $U, V, W$  coordinates are chosen for convenience since they are parallel to the directions of the EC scintillators (and to the EC edges). The cuts have been adjusted by looking at Fig. 3 and making sure the distribution is  $\phi$ -symmetric

$$40 \leq U \leq 400, V \leq 362, W \leq 395$$

The  $U, V, W$  distributions are plotted in Fig. 10,11,12, respectively. In average, 80.9% of all the events with an EC signal pass the U cut, 71.3% the V cut and 69.4% the W cut, for a combined pass/total ratio of 58%. When all other cuts are applied, the U,V,W cuts keep 96.6%, 88.6%, 86.8% events respectively, for a combined effective cut of 77.8% (the product of these numbers is 74.2% but the corners events are correlated).

In Fig. 13 is plotted the Y versus X track coordinate in the EC plane before and after the  $U, V, W$  cuts.

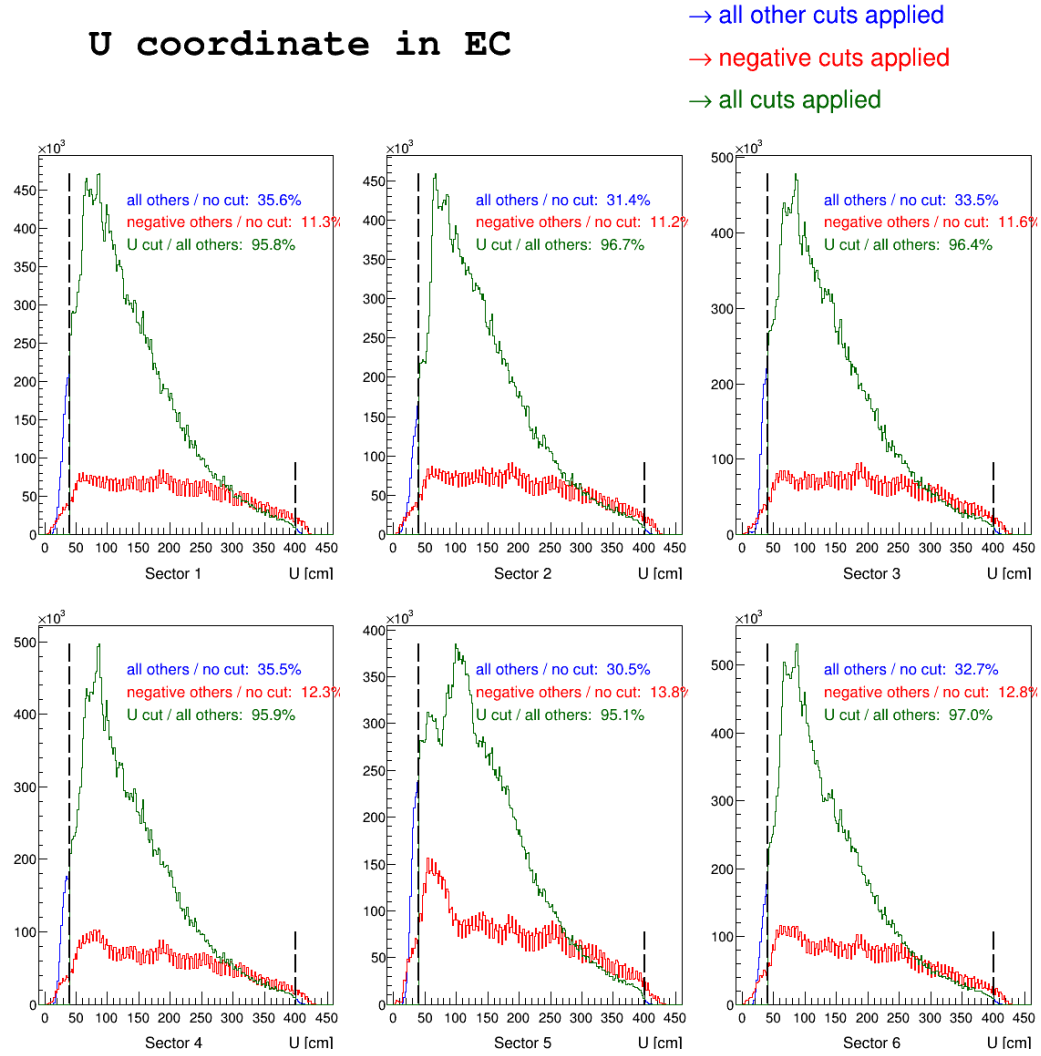


Figure 10: U track coordinate in the EC plane for all sectors. The cut is chosen to avoid edge effects that truncate the electron shower.

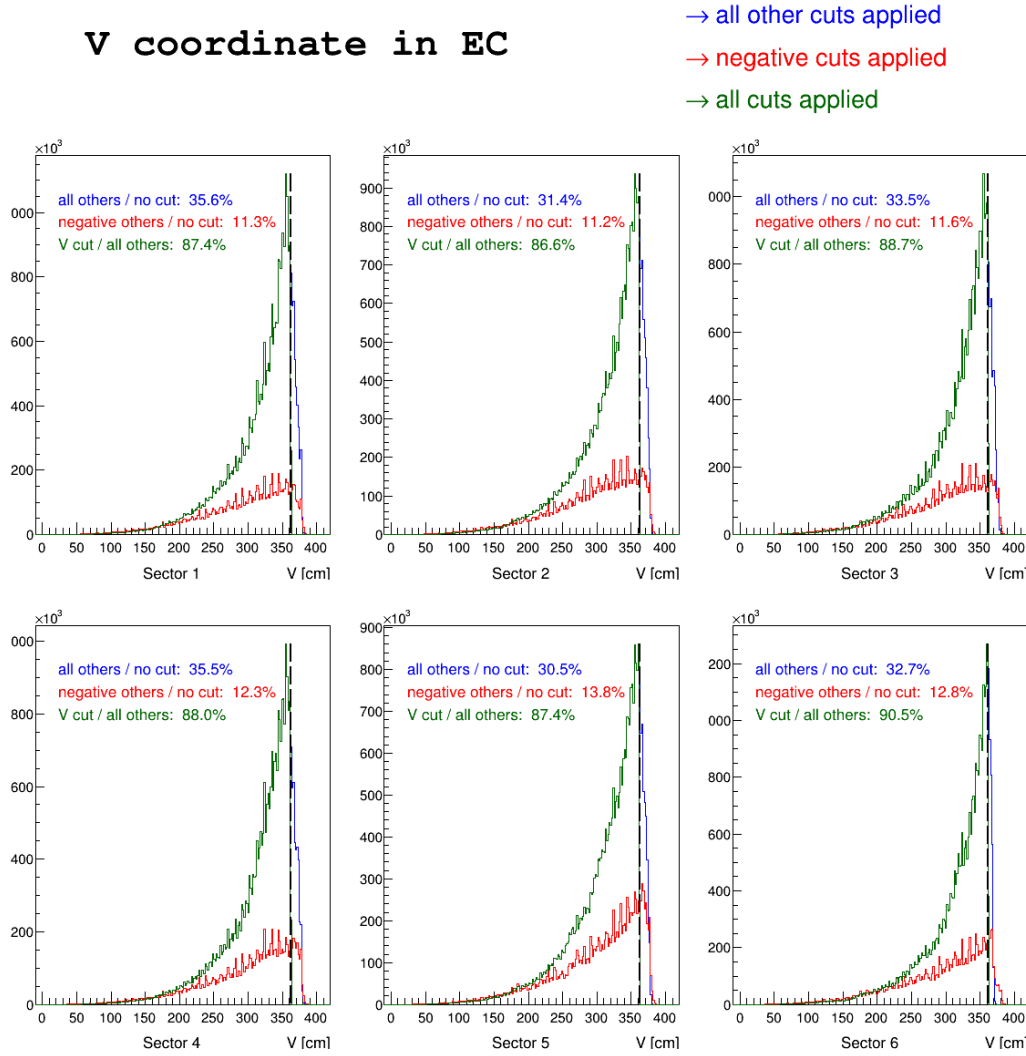


Figure 11: V track coordinate in the EC plane for all sectors. The cut is chosen to avoid edge effects that truncate the electron shower.

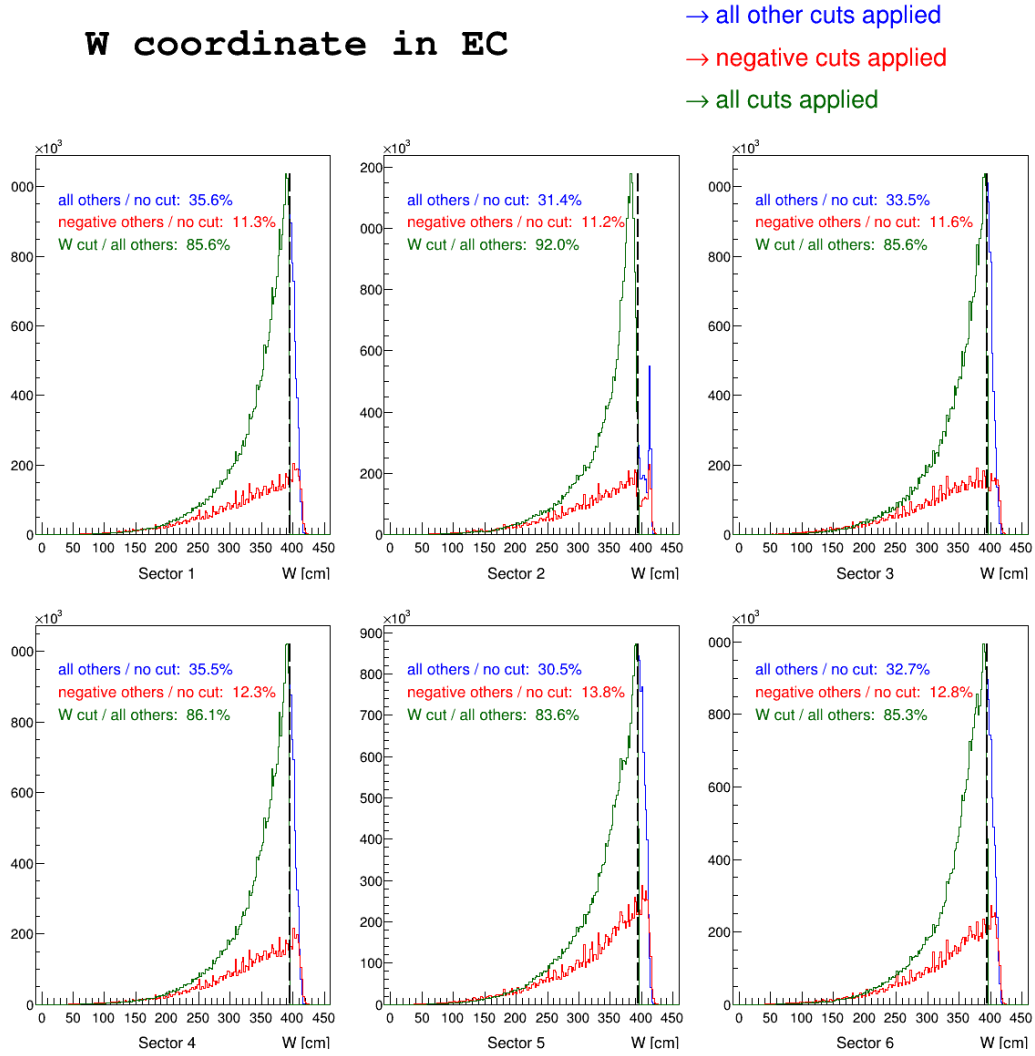


Figure 12: W track coordinate in the EC plane for all sectors. The cut is chosen to avoid edge effects that truncate the electron shower.

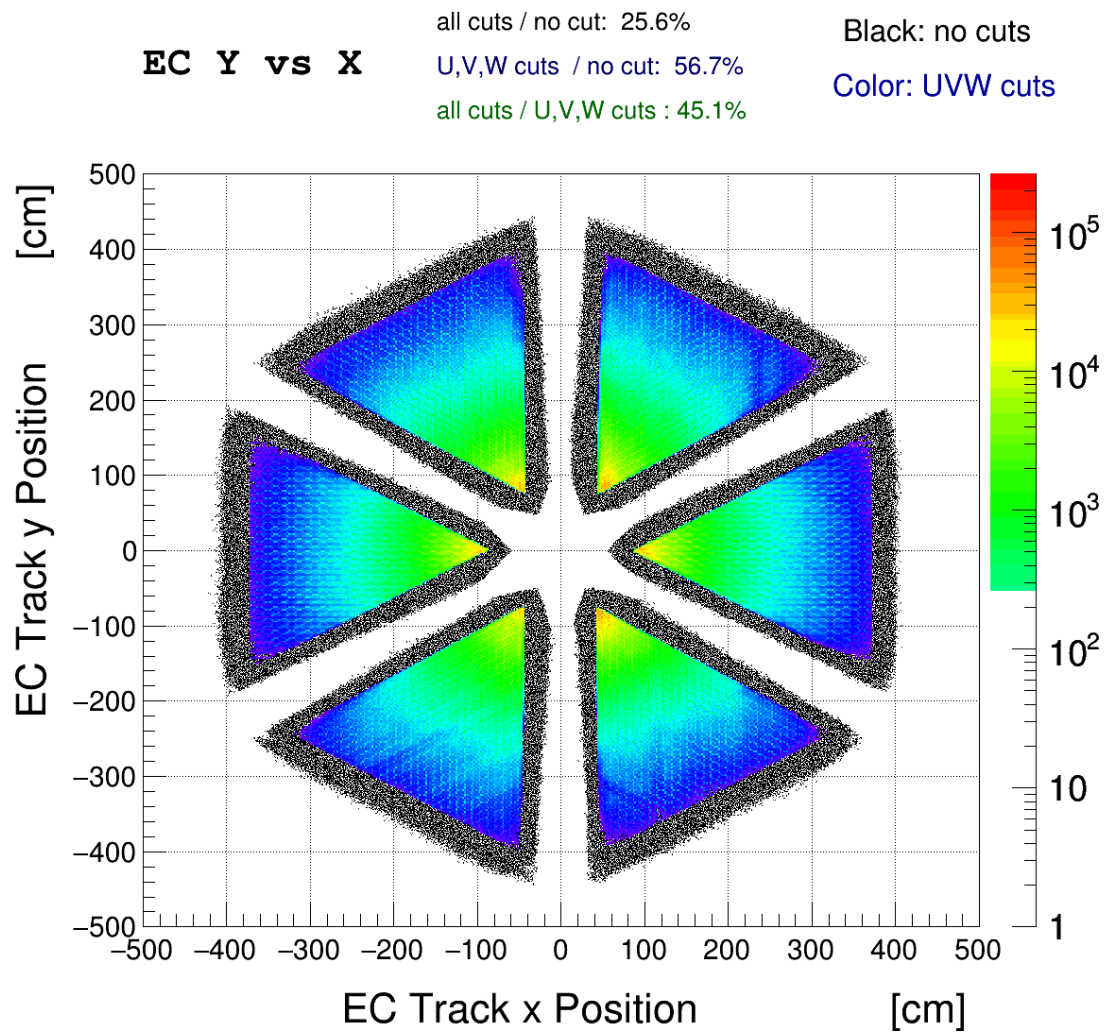


Figure 13: Y versus X track coordinate in the EC plane before and after the  $U, V, W$  cuts.

## 1.7 Minimum Ionizing Particles (MIP) rejection

The outer EC is  $5/3$  times bigger than the inner EC. Therefore pions, which do not shower and are minimum ionizing particles in the momentum range detected in CLAS, release a (small) quantity of energy in the outer and inner parts in the ratio  $5 : 3$ , independent on their momentum.

In Fig. 14 the  $E_{out}/p$  versus  $E_{in}/p$  is shown for Sector 1. One can see the MIP signal along the  $y = 5/3x$  line. Panel b shows the same quantity when all other cuts are applied. One can see that the electron signal on the right. The cut is extrapolated by visually comparing panel a and b and trying to cut the most MIP as possible with a straight line  $y = a + bx$ . The line is sector dependent as shown in Fig. 15. This cut also include a minimum EC outer energy requirement of  $1\text{MeV}$ . The cut values used in each sector and their effectiveness are summarized in table ??.

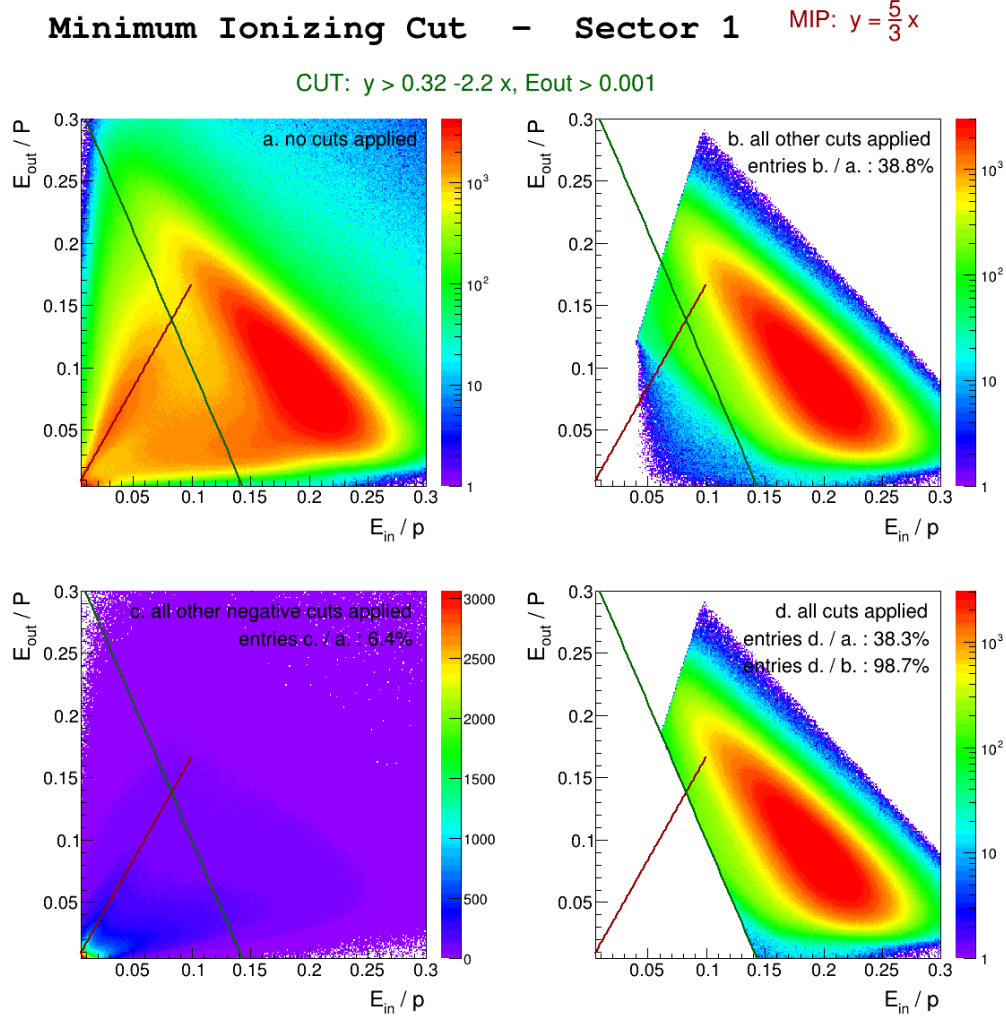


Figure 14:  $E_{out}/p$  versus  $E_{in}/p$  for Sector 1.

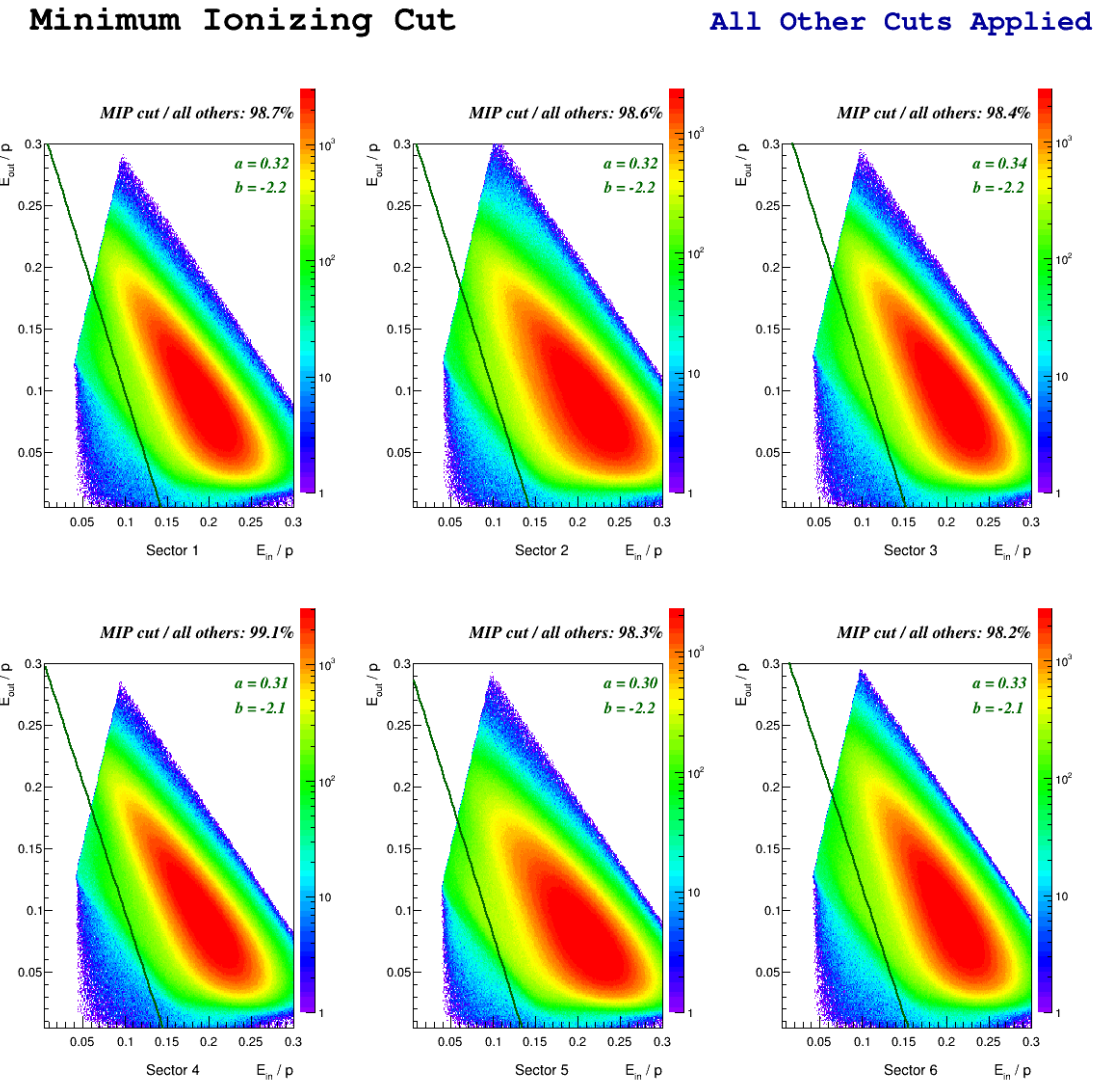


Figure 15:  $E_{out}/p$  versus  $E_{in}/p$  for all sectors. In every sector roughly 99 % of events with all other cuts applied also pass this cut.

Sector	$y = a + bx$ pars	MIP cut / All others %	%
1	$a = 0.32, b = -2.2$	98.7	
2	$a = 0.32, b = -2.2$	98.6	
3	$a = 0.34, b = -2.2$	98.5	
4	$a = 0.31, b = -2.1$	99.1	
5	$a = 0.30, b = -2.2$	98.5	
6	$a = 0.33, b = -2.1$	98.3	

Table 3: The Minimum Ionizing cut values and effectiveness in each sector. The last column refers to events with signal in EC that pass the MIP cut.

## 1.8 Electromagnetic Shower Shape

Due to their shower shape, electrons release more energy in the inner part of the calorimeter than in the outer part. In fact the energy released in the inner part constitutes a good fraction of the total energy in the calorimeter. We chose to keep the events with

$$E_{in}/E_{TOT} \geq 0.25$$

This cut is very loose since most of the MIP are already cut out with all the other cuts, as seen in Fig. 16. This cut keeps more than 99% of events in each sector.

## 1.9 Number of photo-electrons in the Čerenkov detector

In the past a threshold for the signal in the Čerenkov detector was necessary to eliminate electronic noise and the fact that negative pions produce Čerenkov light when their momentum is above  $\sim 2.5$  GeV.

The ADC signal from the CC is converted in number of photo-electrons (nphe) and multiplied by 10. The number of photo-electrons detected in the Čerenkov Counter for electrons is typically between 5 and 20, or  $10 \times nphe_{el} \sim 50 - 200$ . You can see from Fig. 17 the  $10 \times nphe$  distribution in each sector.

The peak at  $nphe \sim 1$  represents not only background and negative pions, but good electrons with low CC efficiency hits. For this reason it's better to apply the CC  $\theta, \phi$  and Timing match cuts.

In average (see Fig. 17) only  $\sim 25\%$  of candidates pass the calorimeter cuts. If applied, the nphe cut would keep  $\sim 90\%$  of them.

The  $nphe$  cut is chosen visually to be at the minimum of the  $nphe$  distribution between the background and electron signals peak.

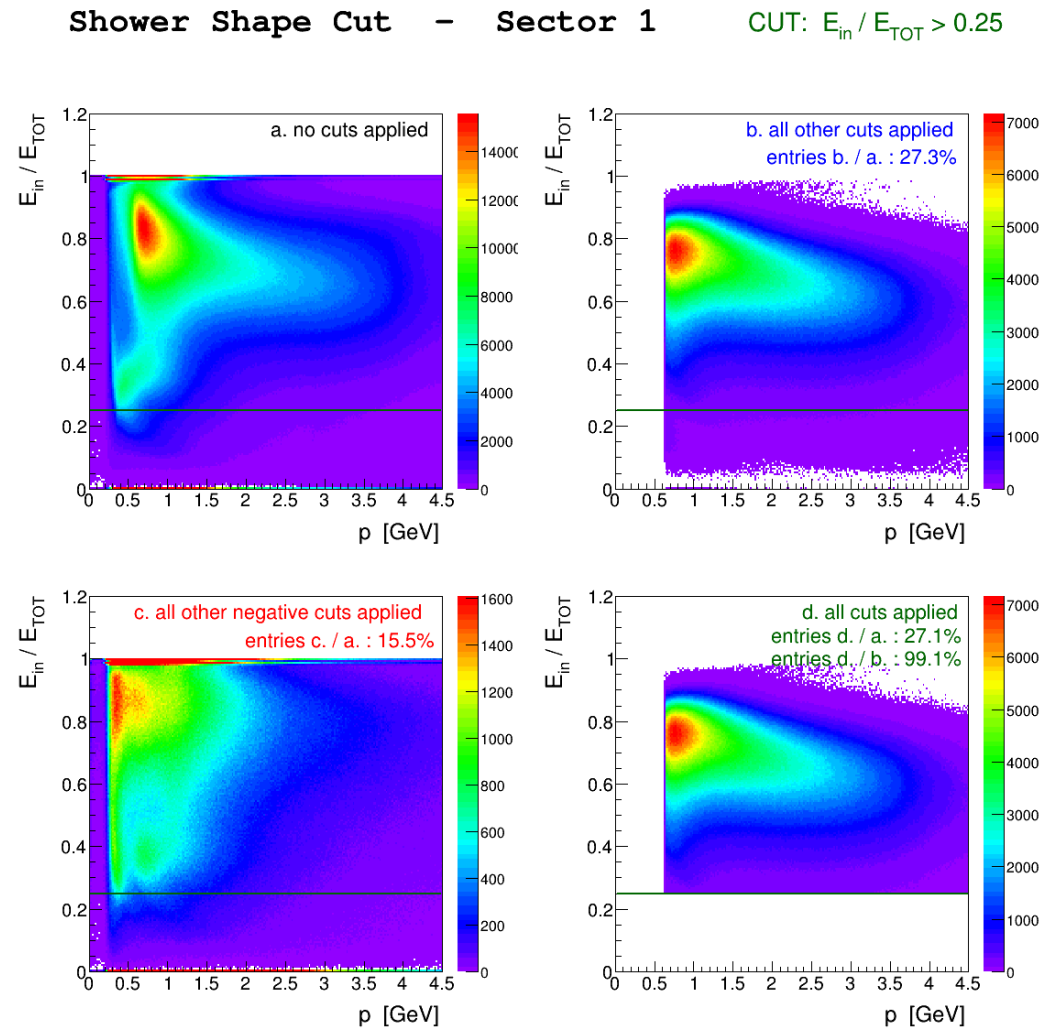


Figure 16:  $E_{in}/E_{TOT}$  for Sector 1. All other cuts (panel b.) almost completely rid of the MIP: 99.1% of those events are kept (Panel d.). Panel c. shows all other negative cuts except the minimum  $p$  cut.

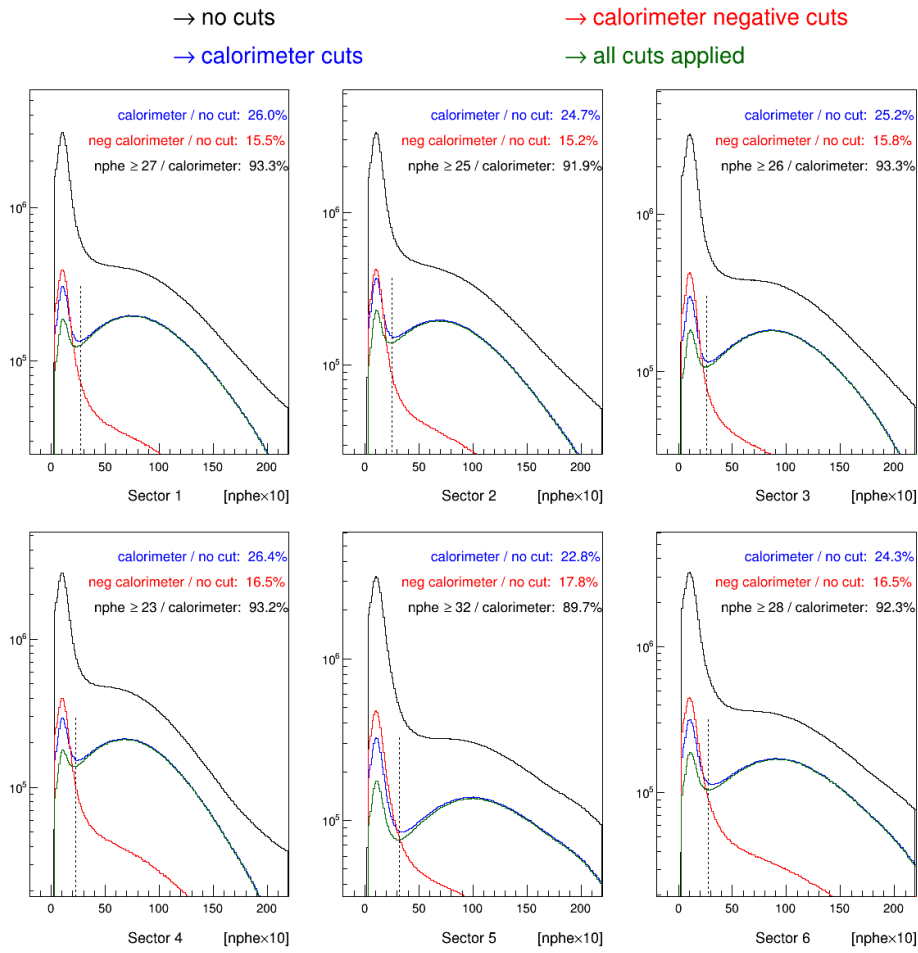


Figure 17:  $10 \times$  Number of photo-electrons distribution integrated over all sectors. In average, only  $\sim 25\%$  pass the calorimeter cuts and of these,  $\sim 90\%$  pass the  $nphe$  cut.

## 1.10 Summary of Electron Identification

In Fig. 18 a summary of the electron identifications cuts in all sectors is shown:

- Individual cuts effect: this is the percentage of events that would be selected by each individual cut if it was the only cut applied.
- Effectiveness: this is the percentage of events that are selected by each individual cut when all the other cuts are effective.
- Cumulative: this is the percentage of events that are selected by each individual cut when they are applied in the order show.

### Electron Identification Summary

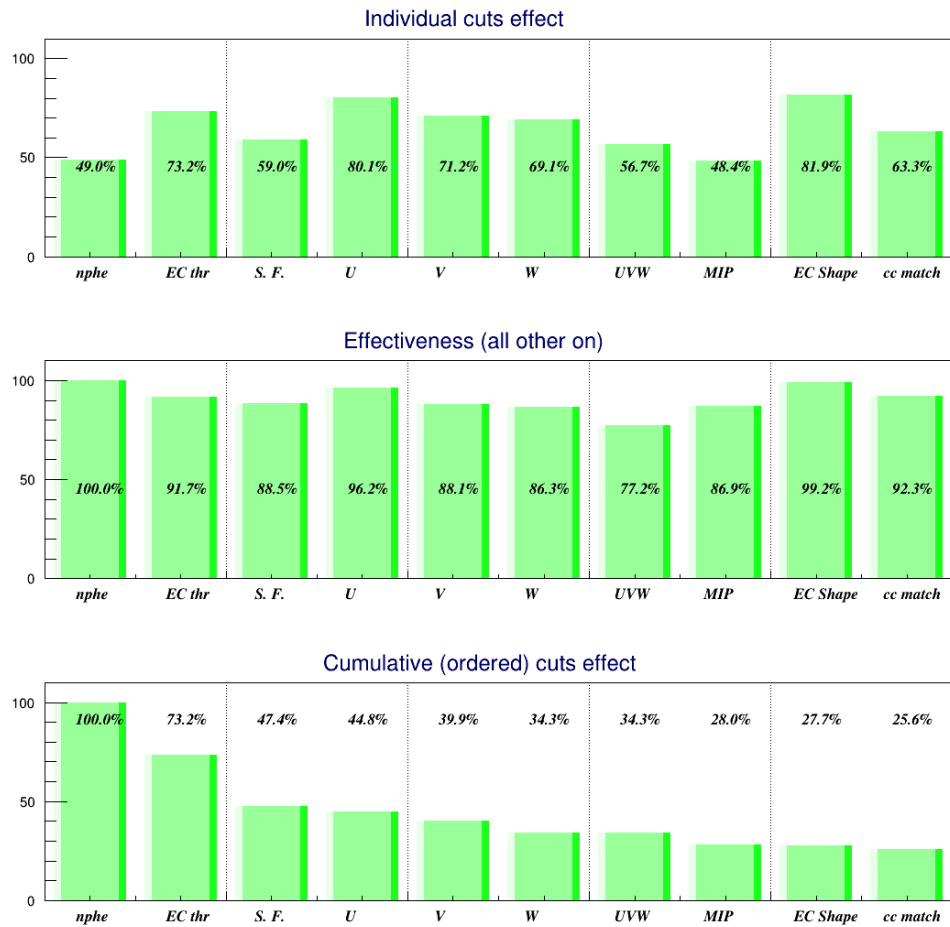


Figure 18: Electron Identification Summary. Top: effects of individual cuts. Middle: effectiveness of each cut. Bottom: effects of accumulated (ordered) cuts.

## 2 Proton identification

The purpose of this study is the proper identification of the scattered protons. The CLAS timing resolution decreases as the particles momentum increases. It is problematic to properly identify charged particles with the timing information alone at very large (greater than 3,4 GeV) momentum. The goal of this analysis is to make the best possible selection of protons, while keeping in mind that further refinements based on individual reactions kinematics will be necessary.

### 2.1 CLAS Timing

During the event reconstruction the momentum of a track is calculated with the tracking procedure [12]. To determine its speed  $\beta$ , the start time  $T_0$  is calculated as

$$T_0 = T_{el} - \frac{\ell}{c} - \frac{z - z_0}{c} \quad (2)$$

where  $T_{el}$  is the electron time from TOF measurement,  $\ell$  is the path length of the electron track from the vertex to its TOF hit,  $c$  is the speed of light,  $z$  is the z-component of the event vertex and  $z_0$  is the  $z$  position of the center of the target<sup>1</sup>.  $T_0$  is then used as the reference for all the remaining tracks in the event. The track speed  $\beta$  is calculated as:

$$\beta = \frac{v}{c} = \frac{1}{c} \frac{\ell}{T - T_0} \quad (3)$$

where  $\ell$  is the track path length from the target and  $T$  its TOF time. In Fig.19 is plotted  $\beta$  versus momentum for the all the particles after the electron particle ID. One can clearly see bands corresponding to pions, kaons, protons, deuterons.

### 2.2 $\Delta T$ cut

For this analysis every positive track (determined by its curvature in the torus field) is a *proton candidate*.

The difference  $\Delta T$  between the time calculated using the candidate's momentum (assuming it is a proton) and its actual TOF time  $T$  should peak at zero for protons:

$$\Delta T = \frac{\ell}{\beta'} + T_0 - T(\sim 0) \quad (4)$$

where  $\beta' = \sqrt{p^2/(M_P^2 + p^2)}$  is the speed of the track calculated from its momentum and  $M_P$  is the proton mass. A plot of  $\Delta T$  versus momentum for Sector 1 is shown in Fig.20. The distribution is sliced along  $\Delta T$  and each slide is fitted with 2 Gaussian + 2<sup>nd</sup> order polynomial function to calculate the mean positions  $\mu$  and sigmas  $\sigma$  of the proton and pions/kaons signals. The proton's  $\mu$  and  $\sigma$  are then fitted with a 5<sup>th</sup>-order polynomial. An example of  $\mu$  fit is also shown in Figures 20 and 21.

At low momentum the protons are well separated. The pions distribution start to contaminate the protons when  $\mu_P + 3\sigma_P < \mu_\pi - 3\sigma_\pi$ ; in that case  $(\mu_\pi - 3\sigma_\pi - \mu_P)/3$  is used as the signal  $\sigma$  instead of  $\sigma_P$ . In Fig.21 the cuts for all sectors are shown.

Two quantities normally used to monitor the quality of the charged particles selection are  $\beta$  and the TOF Mass  $M_{TOF}^2$ :

$$M_{TOF}^2 = \frac{p^2(1 - \beta^2)}{\beta^2}$$

Both  $\beta$  and  $M_{TOF}^2$  versus momentum are shown for sector 5 in Fig.22. The  $M_{TOF}^2$  was initially considered to perform this identification. However, when sliced, the corresponding 1-dimensional plots could not resolve the protons and kaons/pions signal as well as  $\Delta T$  can.

The value of the  $\mu$  and  $\sigma$  parameters used are listed in sec2.2.1.

---

<sup>1</sup>For this experiment  $z_0 = -4$  cm.

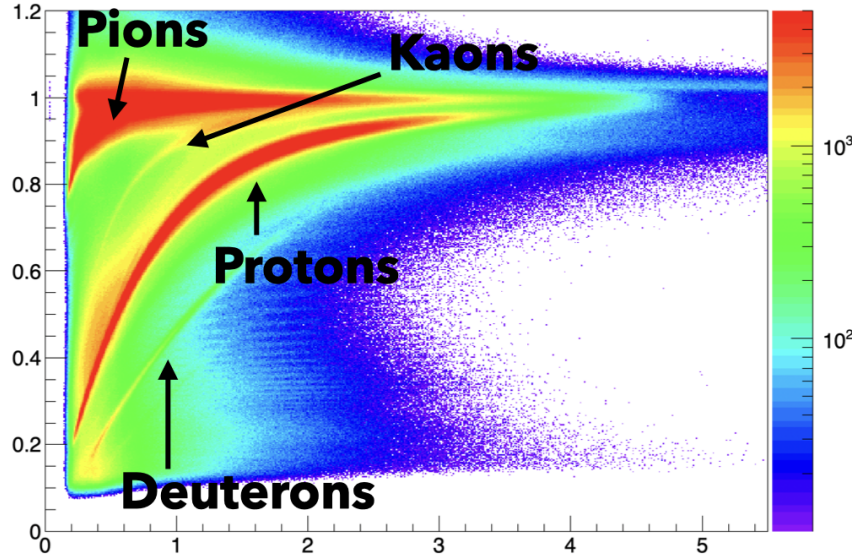


Figure 19:  $\beta$  versus momentum for positive particles in e1-6 running period. Bands corresponding to pions, kaons, protons and deuterons are visible.

### 2.2.1 Cut parameters

$$f(p) = a + bp + cp^2 + dp^3 + ep^4 + fp^5$$

	S1	S2	S3	S4	S5	S6
<b>mean:</b>						
a:	-0.9113	-0.655048	-0.904261	-0.709094	-0.724329	-0.418643
b:	2.98931	1.38425	1.76954	0.591925	4.06097	0.781139
c:	-4.09545	-2.10418	-1.9409	0.272274	-5.8547	-0.943656
d:	2.19893	1.2356	0.948967	-0.454383	3.18819	0.501819
e:	-0.495131	-0.290715	-0.194741	0.158209	-0.720678	-0.117491
f:	0.0389196	0.0232255	0.0136907	-0.0165409	0.0568144	0.00959472
<b>sigma</b>						
a:	6.16714	6.60215	5.87269	5.90242	5.96331	5.99657
b:	-12.1628	-14.4183	-10.6575	-11.7175	-12.2304	-12.4064
c:	9.86015	12.6391	8.00035	9.75136	10.391	10.69
d:	-3.74511	-5.02972	-2.86622	-3.90726	-4.04935	-4.35567
e:	0.679294	0.926557	0.497855	0.750446	0.737621	0.835659
f:	-0.0470408	-0.0639353	-0.033369	-0.0545215	-0.0505353	-0.0600134

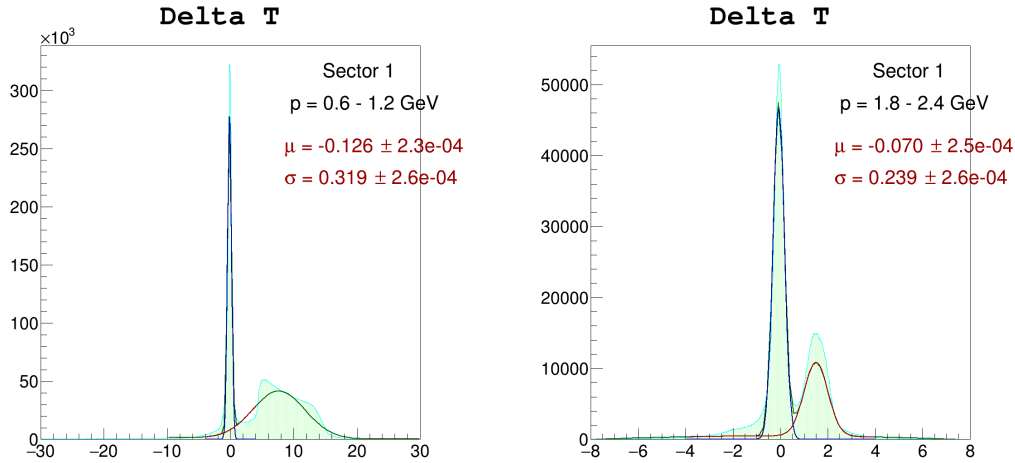
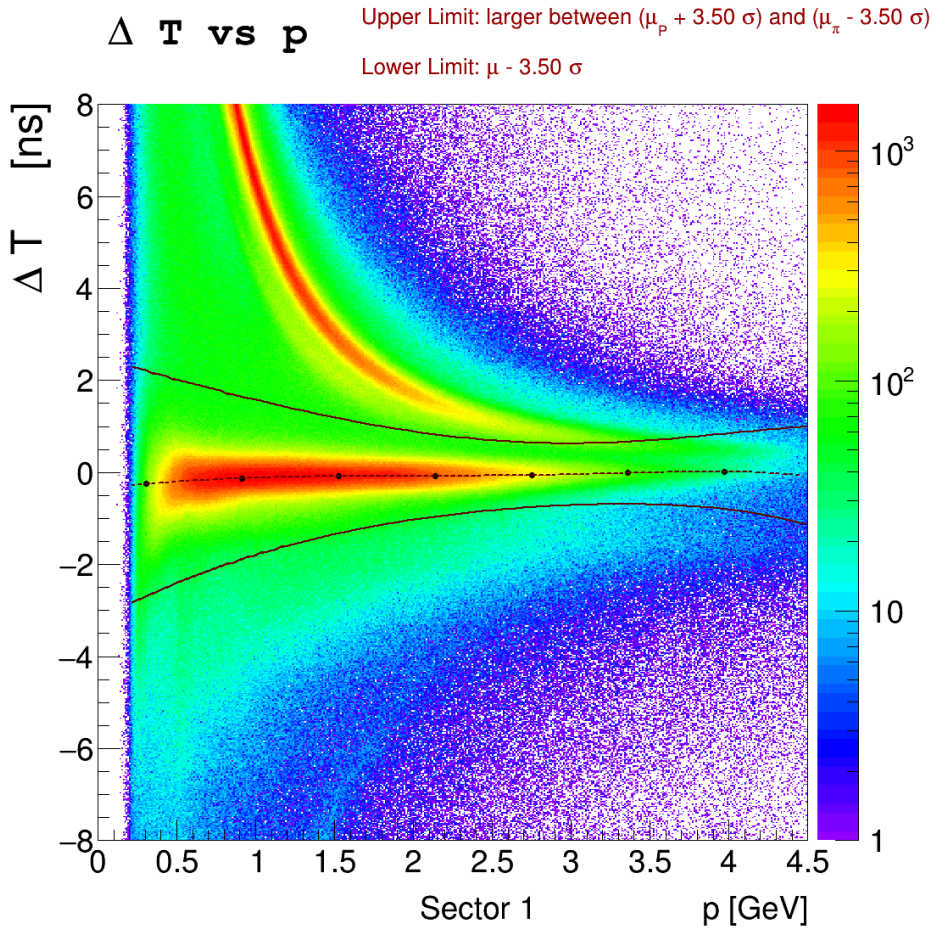


Figure 20:  $\Delta T$  versus momentum and slices at different momentum. At low momentum the proton signal is well separated from kaons and pions, so we include everything up to  $3\sigma$  from the pion/kaons signal. At high momentum kinematic constrains for exclusive channels will be necessary. The colors are as follows: blue: proton signal (gaussian). Red: pion signal (gaussian) + background ( $2^{nd}$  order polynomial). Dark green: total fit function.

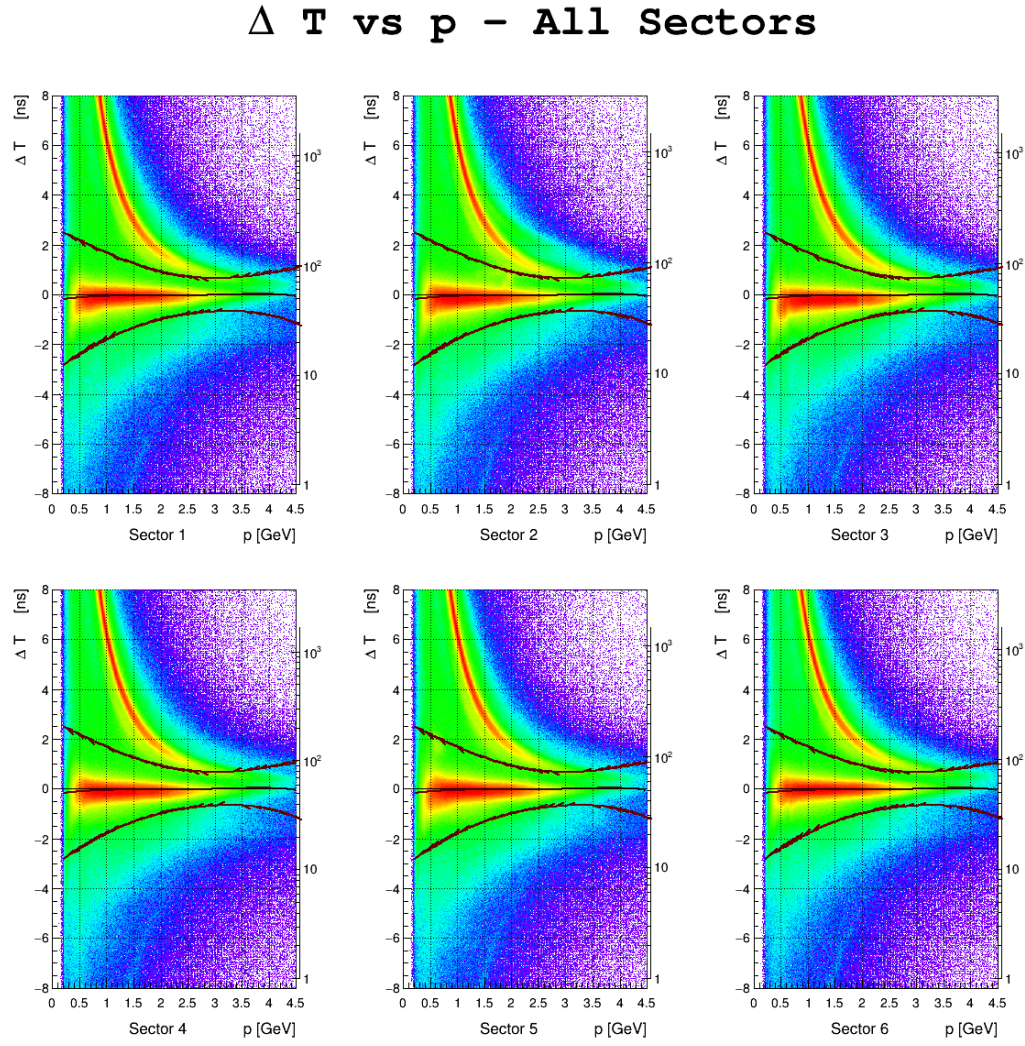


Figure 21:  $\Delta T$  versus momentum cuts in all sectors. Plot grids emphasize the differences between sectors.

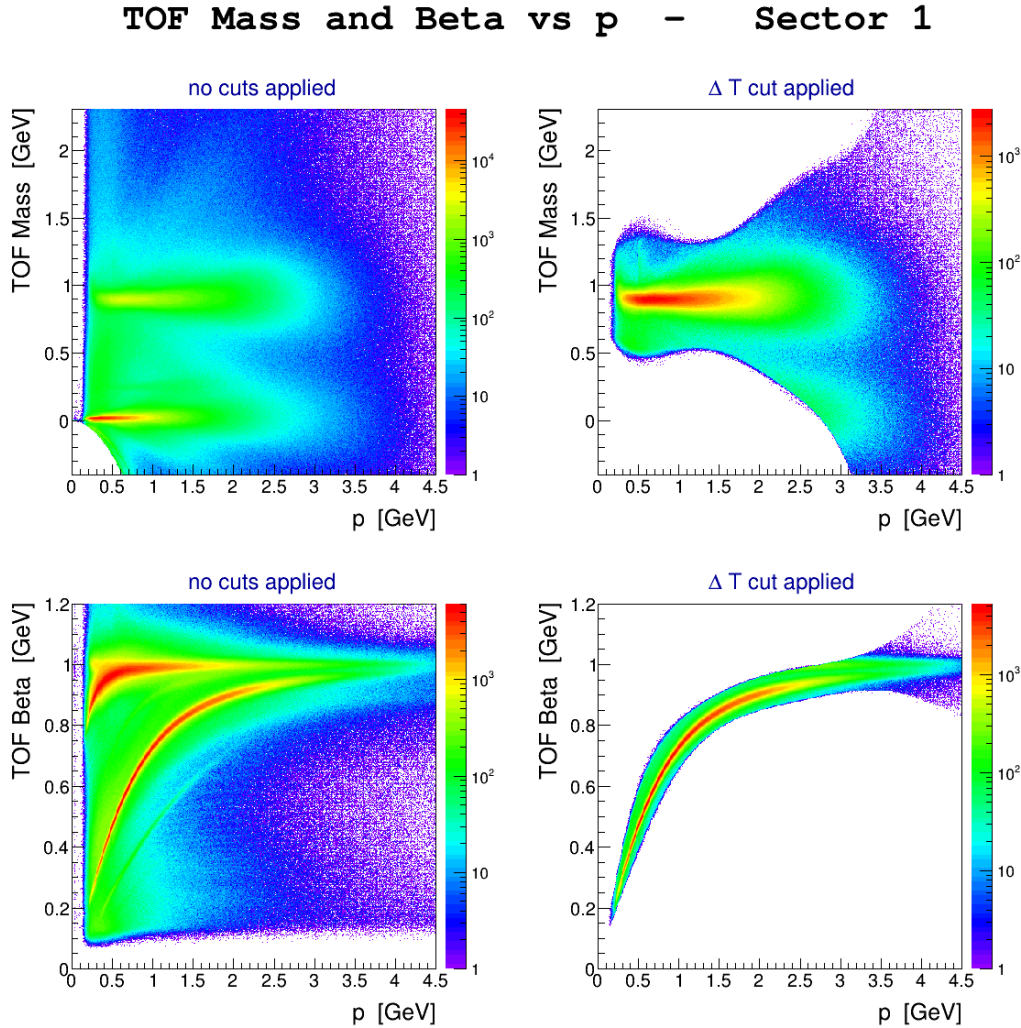


Figure 22: Left:  $\beta$  and  $M_{TOF}^2$  versus momentum for positive tracks with no cut applied. Right: the same quantities with the  $\Delta T$  cut applied.

The complete set of plots can be found on the web [13].

### 3 Vertex Correction, Selection

In the reconstruction software the track vertex ( $x, y, z$ ) is calculated from its intersection with the sector mid-plane<sup>2</sup> of the corresponding sector. This procedure assumes that the beam is centered along the z-axis. However, during the e1-6 experiment the beam was not centered at  $(x, y) = (0, 0)$  thus a sector-dependent offset is introduced in the vertex calculation.

#### 3.1 Beam Offset

The displacement of the beam can be seen in Fig. 23, where the events on the window<sup>3</sup> downstream of the target were selected to fix the z position as reference. The calculated displacement [14] for the beam position is:

$$\begin{aligned} x_0 &= 0.090 \text{ cm} \\ y_0 &= -0.345 \text{ cm} \end{aligned}$$

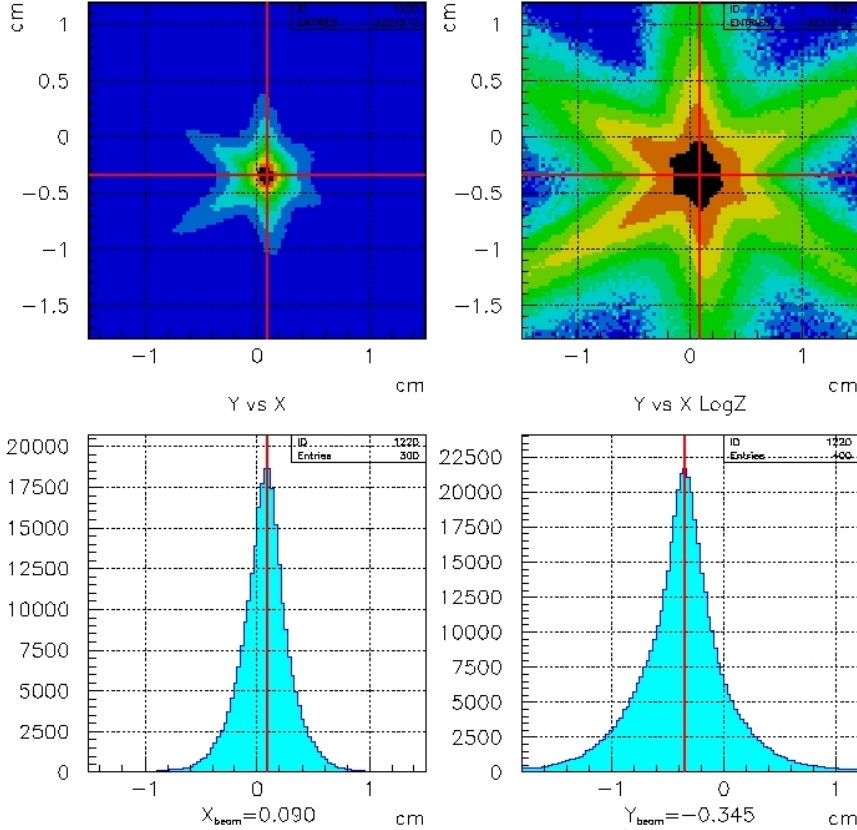


Figure 23: Top:  $y$  versus  $x$  position of the vertex at the window. Upper right: same as upper left, except plotted logarithmically. One can see that the beam spot was slightly shifted from  $(0, 0)$ . Bottom: the  $x$  (left) and  $y$  (right) distributions which led to the calculation:  $(x_0, y_0) = (0.09, -0.345)\text{cm}$

<sup>2</sup>The midplane of a sector is defined by the plane that divide that sector in half and contains the beamline  $(0, 0, z)$ .

<sup>3</sup>A window was placed at  $z = +0.5$  cm to help these kind of studies and to be a z-position reference.

### 3.2 Vertex Correction, Cut

To correct the vertex position it is sufficient to shift the mid-planes so that they contain the correct beamline  $(0.09, -0.345, z)$  and recalculate the intersection of the tracks with the new planes. This is illustrated in Fig. 24.

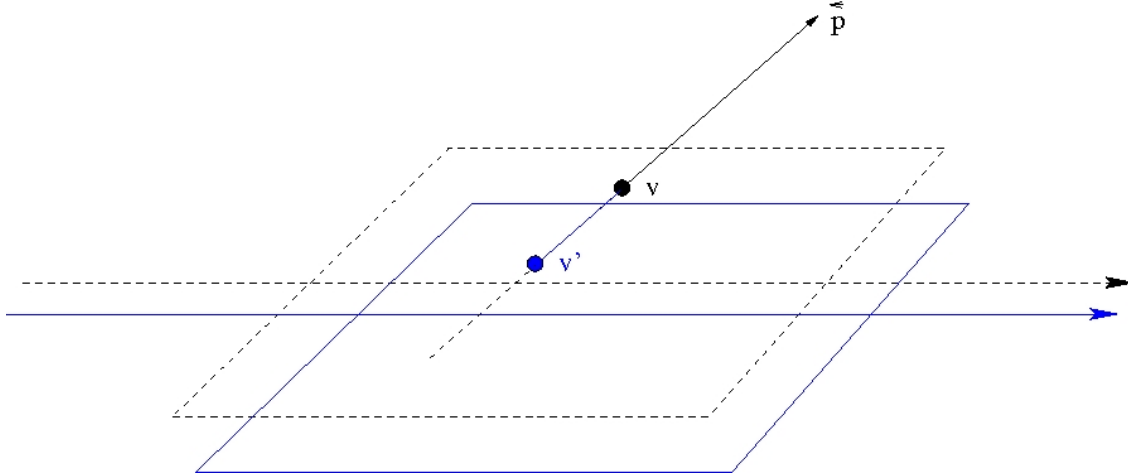


Figure 24: The vertex correction. The dashed plane is the original midplane containing the wrong beamline  $(0, 0, 0)$ . The point  $v$  is the intersection of the track (straight line along momentum  $\vec{p}$ ) with this plane. The solid blue plane represents the corrected midplane containing  $(0.09, -0.345, z)$ . The correction algorithm simply intersects the same track with the corrected midplane.

The effect of the correction on the electrons and protons  $z$  position is shown in Fig. 25. After this correction, the vertex position resolution is good enough to introduce a cut on the  $z$  vertex of electron and protons in order to select events inside the target cell as follows:

$$-8 \text{ cm} \leq z \leq -0.8 \text{ cm} \quad (5)$$

The electron and proton vertices are also required to be coincident along the  $z$  axis within the reconstruction resolution, so an additional cut on  $\Delta z = z_{\text{electron}} - z_{\text{proton}}$  is applied:

$$|\Delta z| < 3 \text{ cm} \quad (6)$$

The effect of the corrections and the values of the cuts are illustrated in Fig. 25 and Fig. 26.

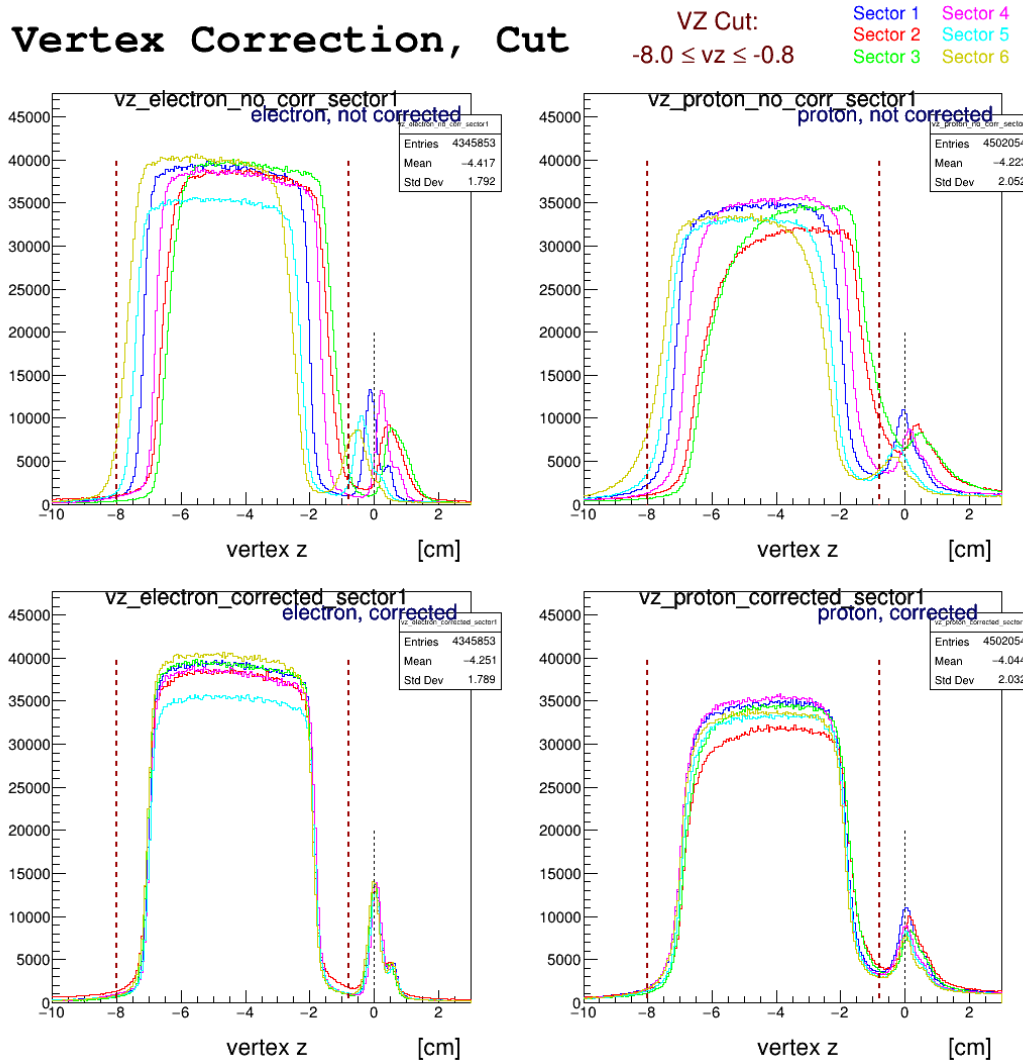


Figure 25: The effect of the correction on the electrons and protons z distributions for each sector. Top row: electron and proton z vertices, uncorrected. Bottom row: same distributions after the vertex correction. Vertical red lines: cuts of eq.5.

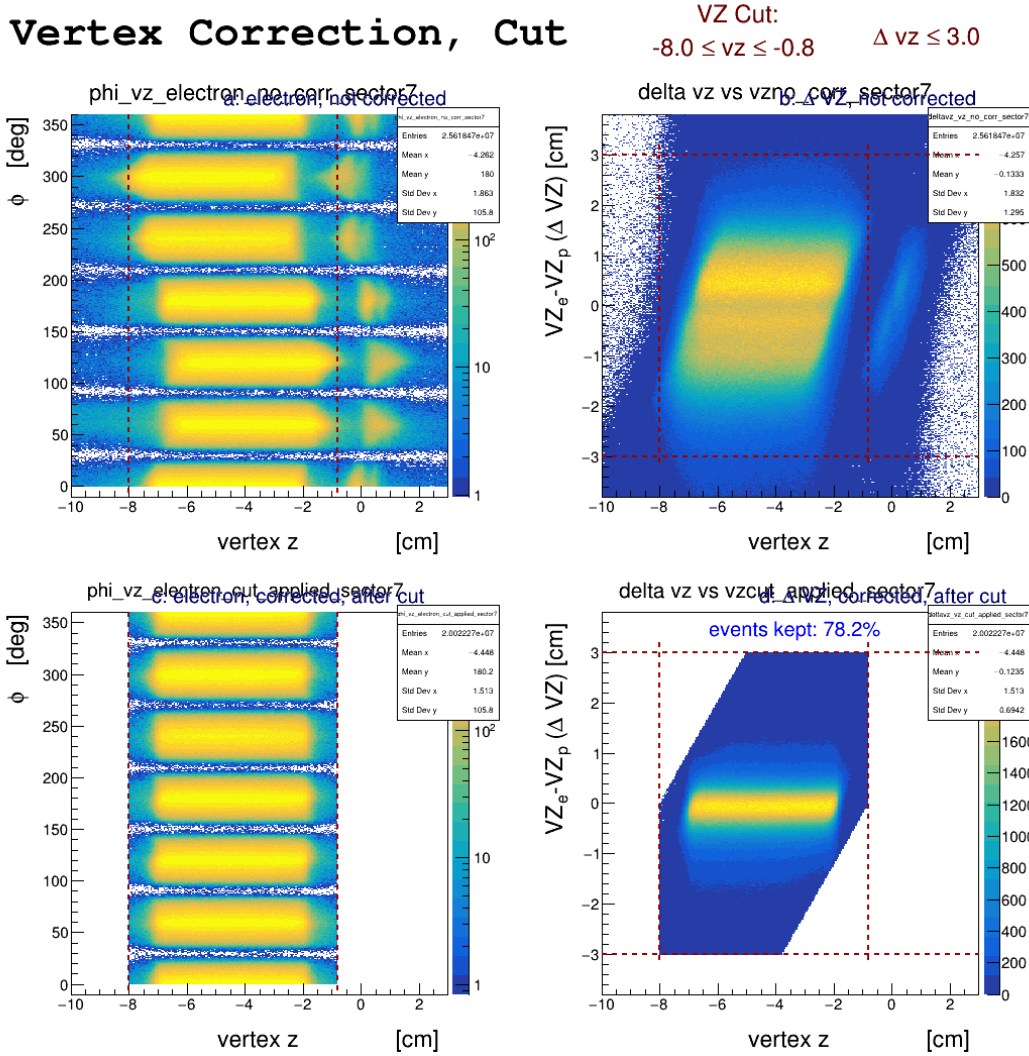


Figure 26: Top left:  $\Delta z$  versus  $\phi_{electron}$ , uncorrected. The typical sinusoidal behaviour as a function of sector is indicative of the beam displacement. Bottom left: same distributions, after the vertex correction. Top right:  $\Delta z$  versus  $VZ_{electron}$ , uncorrected. Bottom right: same distributions, after the vertex correction. Vertical red lines: cuts of eq.5. Horizontal red lines: cuts of eq.6.

## 4 Fiducial Cuts

### 4.1 Introduction

A fiducial cut on electrons is introduced to constrain regions of phase space where the CLAS response peaks at its maximum and remains rather smooth. Furthermore, some detector inefficiencies are not perfectly reproduced with GSIM and need to be removed with dedicated cuts.

The fiducial regions were traditionally defined in the lab coordinates of the electron reconstructed  $\phi, \theta, p$ . However, it is more natural to define the fiducial regions in the detector coordinates, because the inefficiencies are caused by tracks near their borders or hardware problems.

Since the original approach has been used in several published CLAS papers, we will include it in this note as a reference.

### 4.2 Traditional cuts on the electron lab coordinates $\phi, \theta, p$

The fiducial cut in the lab coordinates has been determined during the  $\pi^0$  analysis in the  $\Delta(1232)$  region [17]. For each sector, an empirical cut on  $\phi$  is introduced as a function of theta and momentum:

$$\phi \leq \Delta\phi(\theta, p)$$

which is aimed to define regions of phase space whose distributions are flat in  $\phi$ . After careful studies, and following a common approach between different CLAS experiments, the mathematical form of the cut depends on 6 parameters  $C_i$  and assumes the form:

$$\begin{aligned} \Delta\phi &= C_4 (\sin(\theta - \theta_{cut}))^E \\ E &= C_3 p^{C_5} \\ \theta_{cut} &= C_1 + \frac{C_2}{p + C_6} \end{aligned}$$

The  $\phi$  vs  $\theta$  distribution were divided in 10 different momentum bins from 1.6 to 4.6 GeV. Fig. 27 shows one example ( $p = 1.9 - 2.2$  GeV) of such distributions. The  $\phi$  distributions are also plotted for  $\theta$  slices one degree wide as in Fig. 29 and the  $C_i$  parameters are adjusted empirically.

Table 4 shows the 6 parameters obtained. Fig. 28 shows the fiducial cut as a function of  $p$ ,  $\theta$  and  $\phi$  for sector 1.

Sector	$C_1$	$C_2$	$C_3$	$C_4$	$C_5$	$C_6$
1	12.0	20.0	0.32	32.0	0.416667	0.14
2	//	20.7	0.36	34.0	//	//
3	//	20.2	0.32	32.0	//	//
4	//	20.5	0.32	32.0	//	//
5	//	20.5	0.29	32.0	//	//
6	//	20.0	0.32	32.0	//	//

Table 4: The 6 parameters for electron fiducial cut for each of the 6 sectors. Only  $C_2$ ,  $C_3$ ,  $C_4$  are sector dependent.

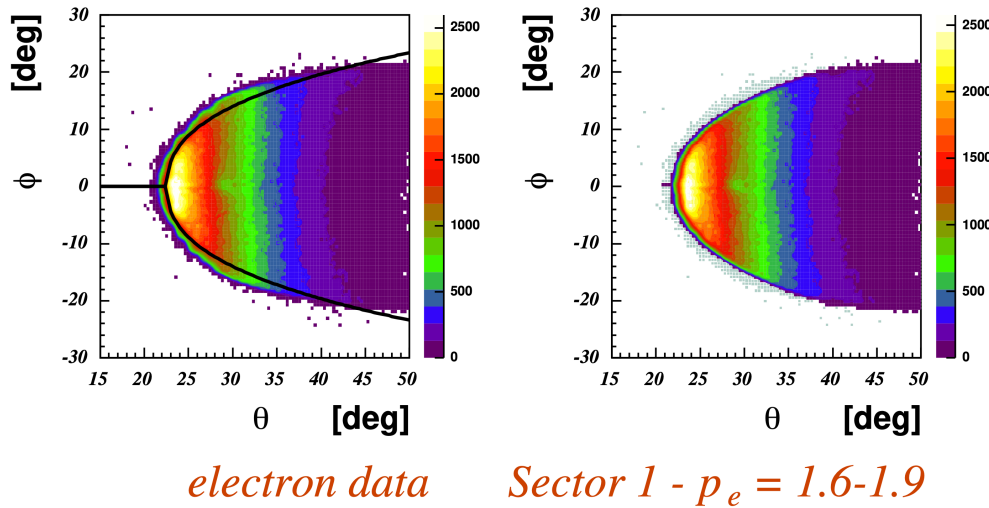


Figure 27:  $\phi$  versus  $\theta$  for sector 1 and  $p = 1.6 - 1.9$  GeV after the electron ID. Left: before fiducial cut. Right: before fiducial cut (box/gray) and after fiducial cut (color contour).

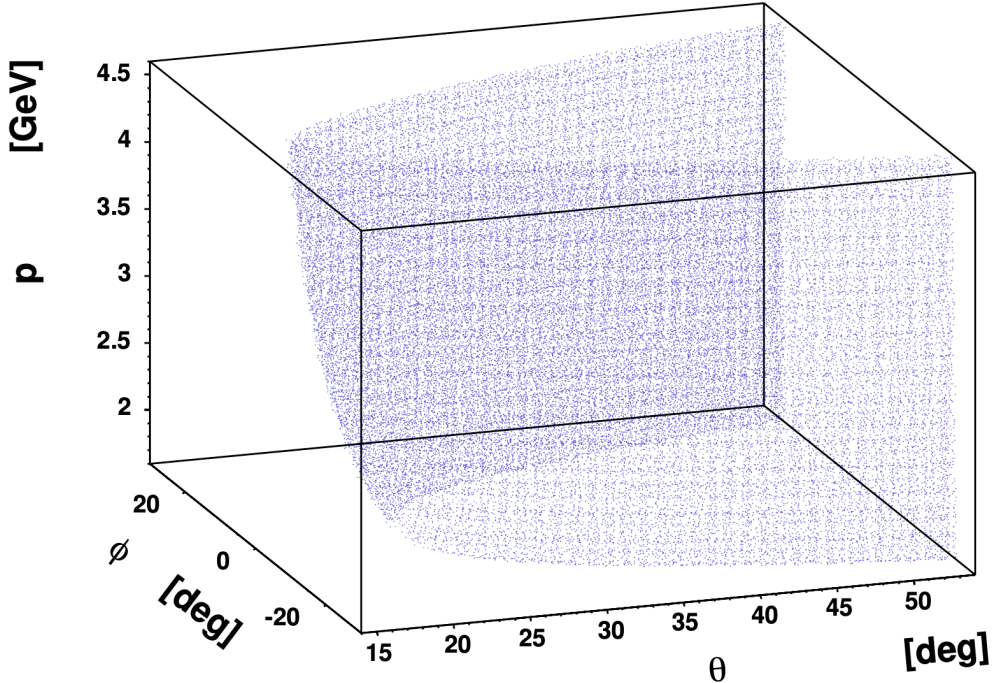


Figure 28: The electron fiducial cut for sector 1 as a function of  $\phi, \theta, p$ . The cut starting point moves back as the momentum increases (and  $\theta$  decreases). This causes the cut to narrow up with momentum because electrons are detected near the lower edges of the detectors.

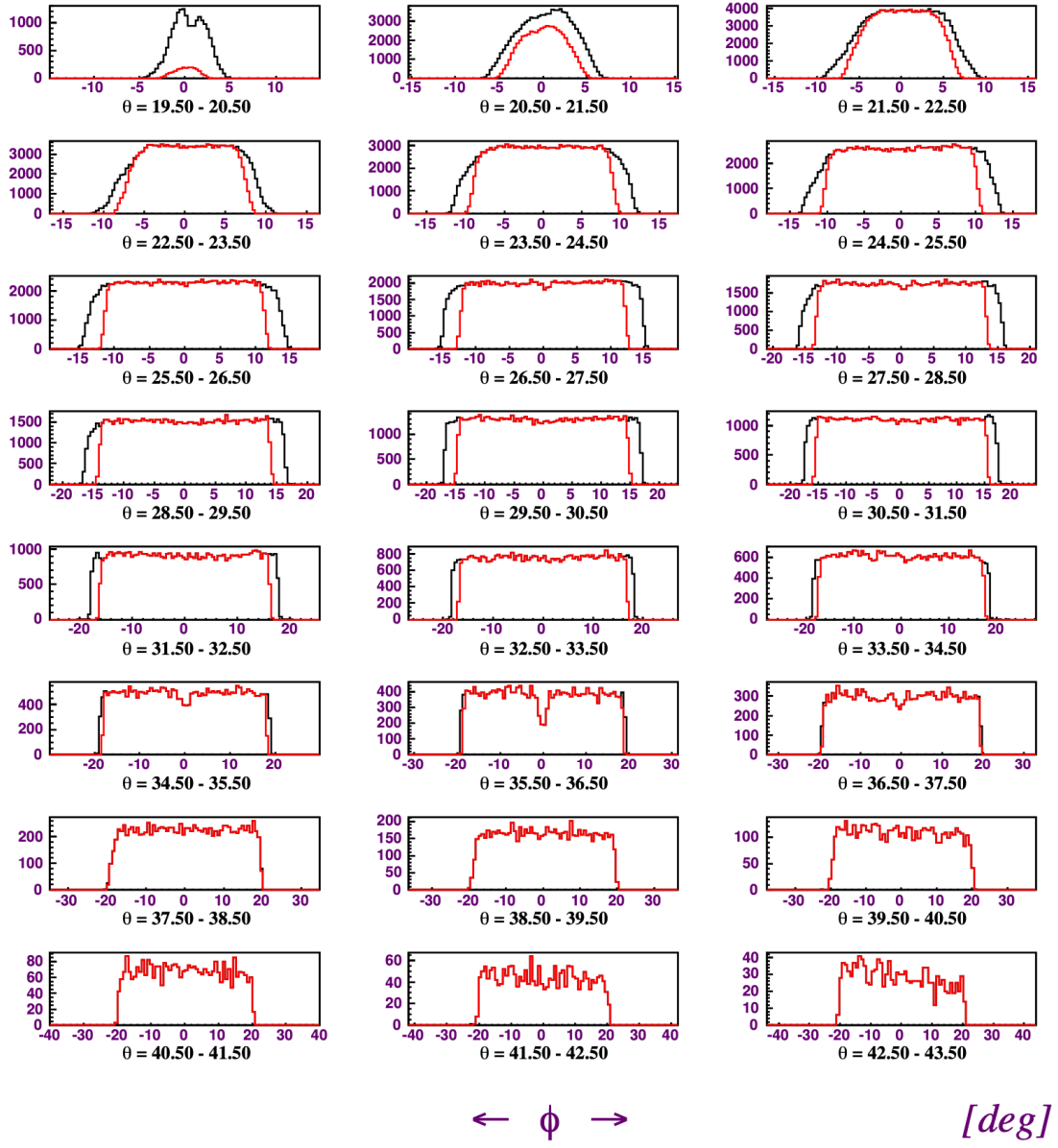


Figure 29:  $\phi$  distributions (sector 3) for different  $\theta$  and  $p = 1.9 - 2.2$  GeV. Black: before fiducial cut. Red: after fiducial cut. Čerenkov inefficiency is responsible for some irregularities at  $\phi = 0$  (for example at  $\theta = 35.5^0 - 36.5^0$ ) while drift chambers and time of flight inefficiency caused other irregularities (for example at  $\theta = 42.5^0 - 43.5^0$ ).

### 4.3 $\theta$ versus momentum cuts

Sector 2, 5 and 6 present holes and depletions (mainly because of dead time of flight paddles) which were taken care of with the cuts in the  $\theta$  vs  $p$  plane. An example of such cut is shown in Fig. 30. The shortcomings using the electron track lab kinematics variable is particularly evident in these  $\theta$  versus momentum cuts: there is no basis for the functions utilised and their distances from the depletions, other than their empirical (visual) approximation.

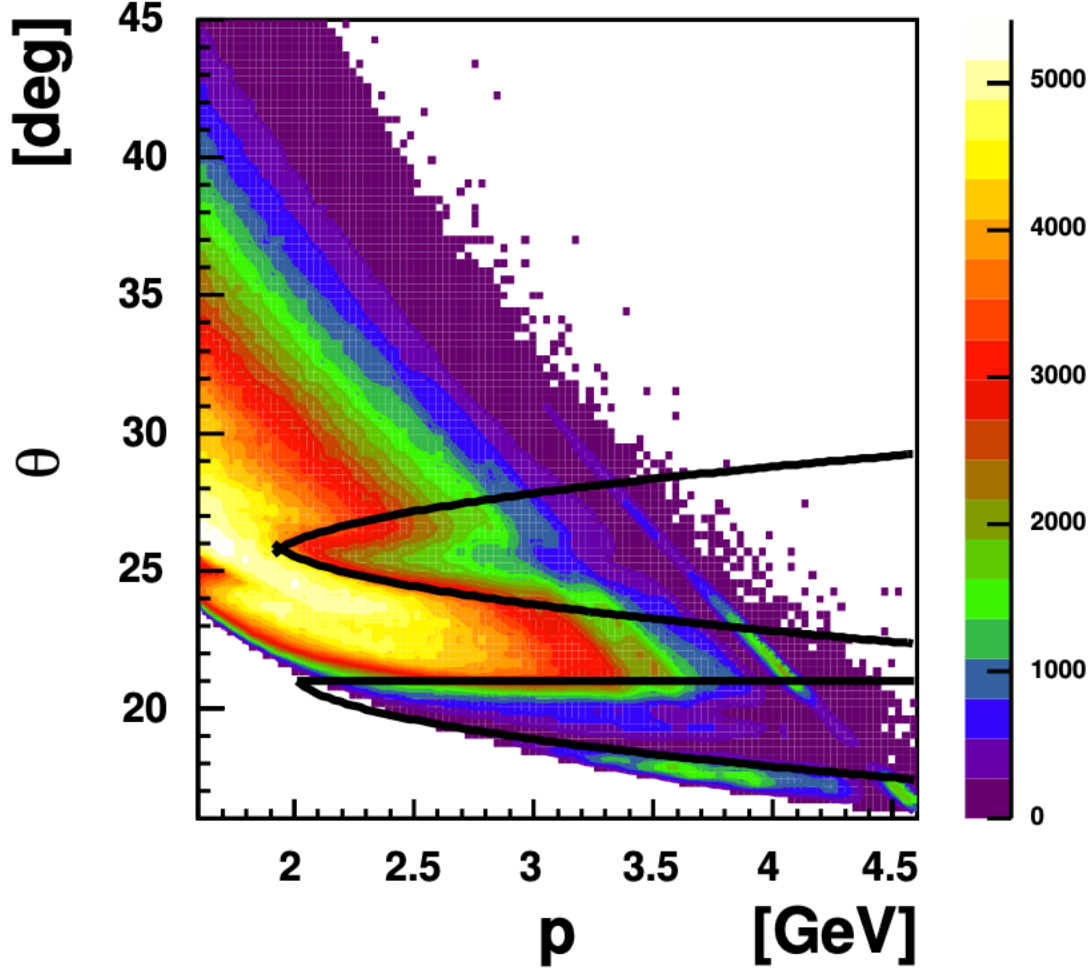


Figure 30:  $\theta$  versus  $p$  for sector 5. Two depletions are clearly visible and cut out.

### 4.4 Cuts on detectors coordinates

As the electrons swim through the detectors, they are subject to inefficiencies near the sector edges. This applies to the 3 regions of the drift chambers (DC1, DC2, DC3) and the time of flight detector plane (SC). An edge cut for the calorimeter was already applied in the electron ID.

The X vs Y distributions of the electron tracks in the DCs and the SC planes in sector 1 are shown in Fig. 31. This section describes the algorithm used to select the high occupancy regions edges.

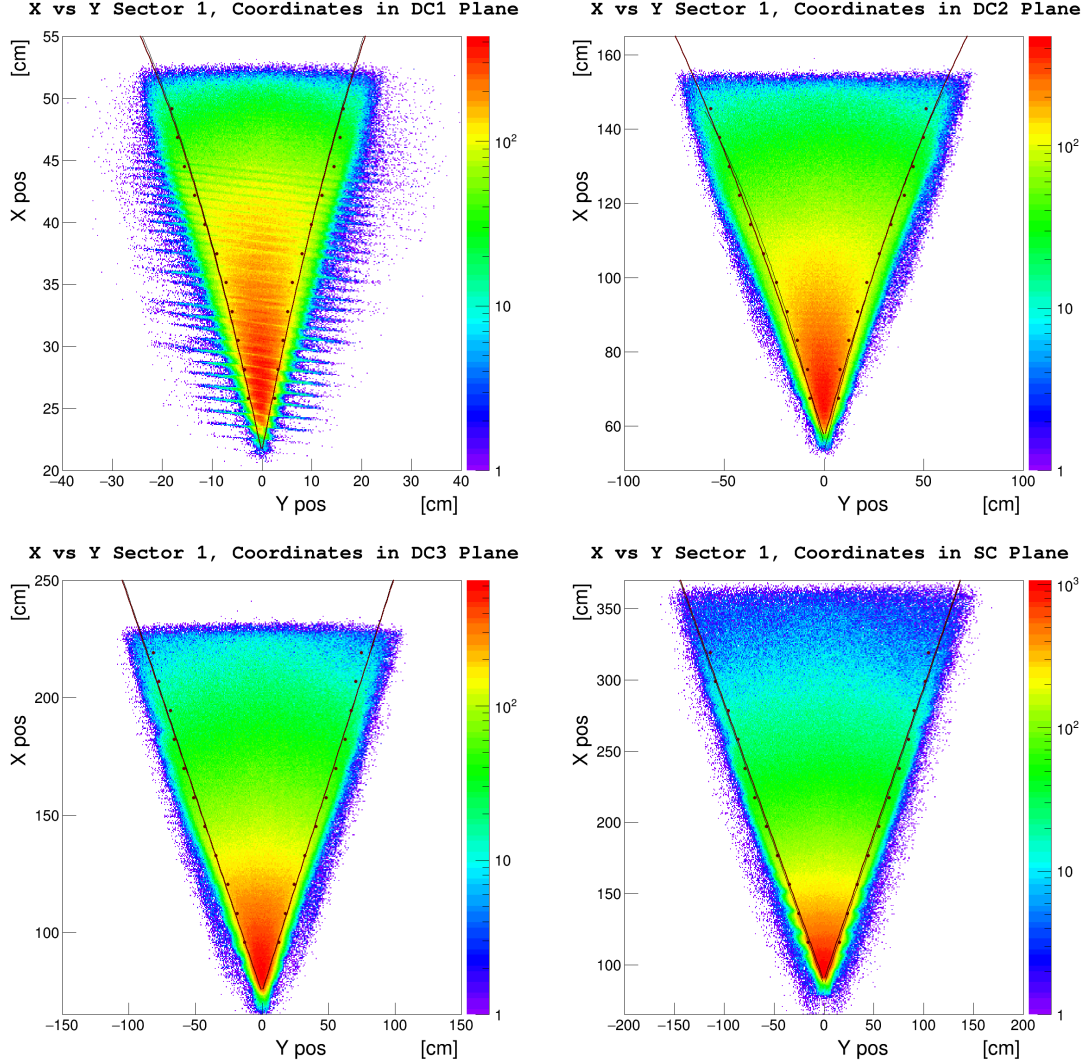


Figure 31: The X vs Y distribution of the tracks in the drift chambers and the time of flight detector plane (SC) for sector 1. The edges selection algorithm described in the text resulted in the black lines, which are the fit of the Y distributions for each X bin.

In each sector and each plane, 12 bins in X are defined; in each bin, the Y distribution is fitted with a “tent” function  $t(y)$  (defined in appendix .1 ) to select the high efficiency edges. An example of such fit is shown in Fig. 32 for sector 1 in the DC3 plane, for 4 bins in X. The fit cleanly identifies the steep rises and falls of the distributions and the relatively flat regions in between.

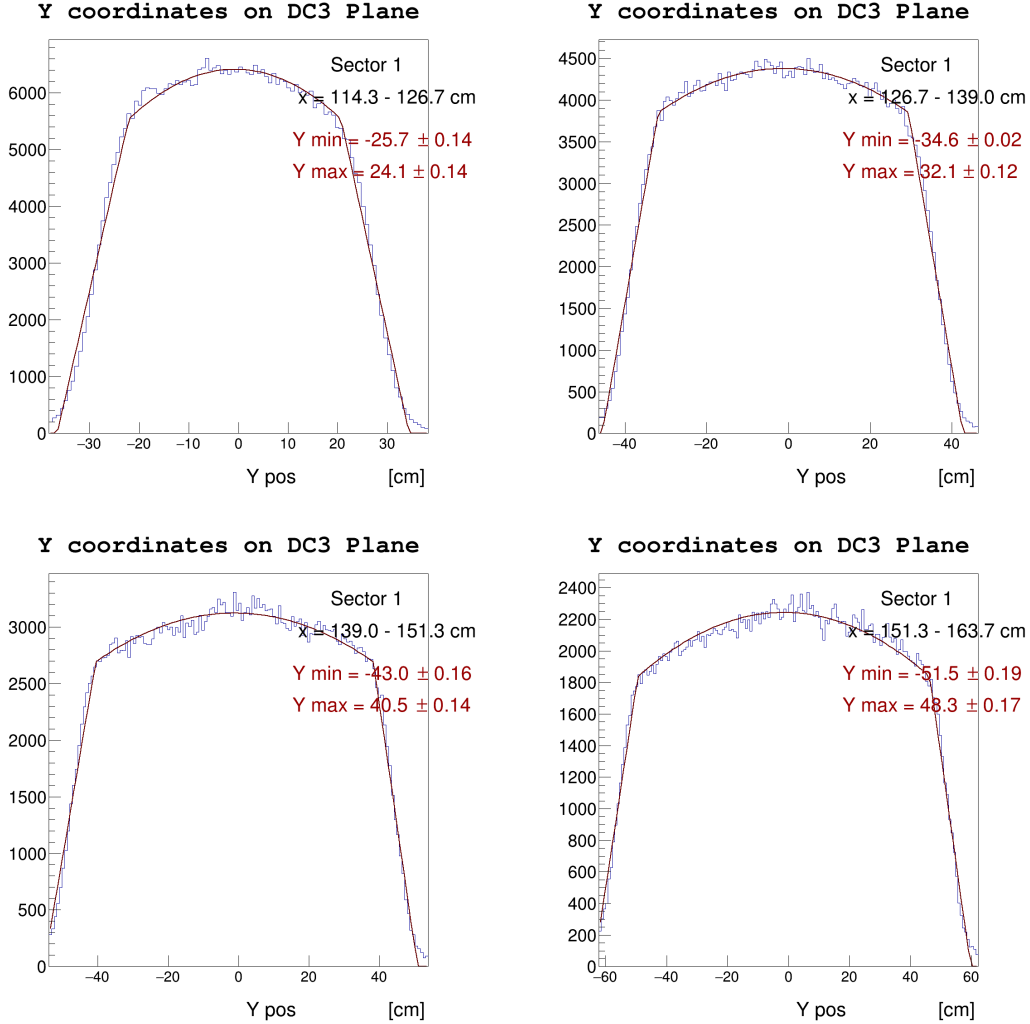


Figure 32: Y distribution for 4 X bins in the DC3 plane for sector 1. The black lines are the tent fit of the Y distributions. The result of the first is the two points of intersection between the straight lines (steep rise) and the parabola fit (flat region). The two points are then plotted in the XY plane and fitted with a parabola, see for example Fig. 31 or Fig. 33.

The results of the tent fit are the two points of intersection between the straight lines (steep rise) and the parabola fit (flat region). The two points are then plotted in the XY plane for all the X bins and fitted with a parabola, see for example Fig. 31 or Fig. 33.

This procedure results in a fiducial cut function for each plane and each sector.

#### 4.4.1 Detectors inefficiencies

The detector coordinates plots allow to correlate hardware inefficiencies with depletions in the XY distributions. For example, in the DC planes, where neighboring group of wires are powered by the same HV supply and axial and stereo wires are tilted by  $6^0$  with respect to each other, the inefficiencies will appear as:

- Axial wires: horizontal bands in the XY distributions
- Stereo wires:  $6^0$  tilted bands in the XY distributions

Three examples of such hardware problems in sector 5 are summarized in Fig. 33. These regions are removed with dedicated cuts represented by straight lines in the XY plane, horizontal for the axial wires and  $6^0$  tilted for the stereo wires.

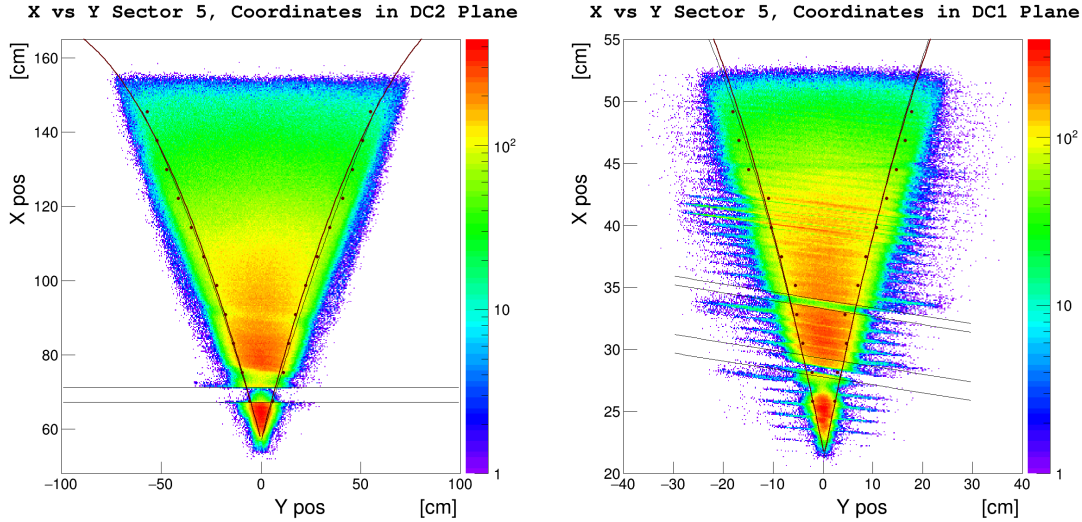


Figure 33: The X vs Y distribution of the electron tracks intersection with the DC2 (left) and DC1 (right) planes in sector 5. The left distribution shows one depletion for the stereo wires, while the right distribution shows two depletions for the axial wires.

#### 4.4.2 Comparison with the traditional cuts

The effect of the fiducial and inefficiencies cuts are compared with the traditional  $\phi, \theta, p$  cuts. The comparison highlights the advantages of the new approach:

- identify the real edge effects in the detector
- hardware problems are represented by straight lines in the XY plane
- no momentum dependence of the cuts

This comparison is shown as an example for sector 5 and a momentum bin in Fig. 34. The before and after  $\phi$  vs  $\theta$  distributions in sector 5 for all the momentum bin are shown in Fig. 35 and 36 respectively.

The complete set of plots is available at [\[16\]](#).

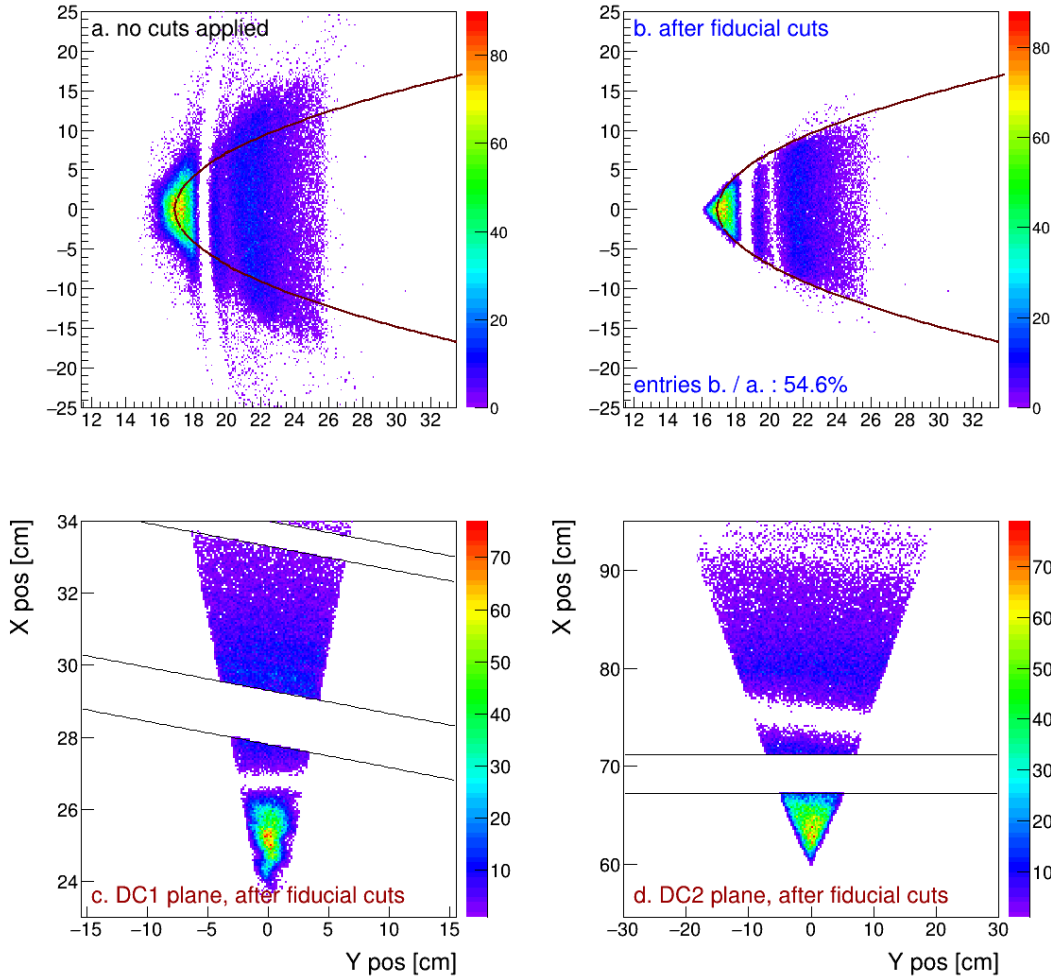
**Fiducial Cut – Sector 5 – Momentum:  $3.8 \pm 0.24$  GeV**


Figure 34: Comparison between the traditional cuts (function of  $\phi, \theta, p$ ) and the new cuts on the XY detector coordinates. Top left:  $\phi$  vs  $\theta$  before any cuts. Top right:  $\phi$  vs  $\theta$  after the XY cuts. The traditional cuts superimposed and shown with black lines. Notice that the traditional cuts would remove events at very small  $\theta$  and large  $\phi$ , due to its functional form. Bottom left: DC1 plane after the fidu XY cuts. Bottm right: DC2 plane after the fidu XY cuts. Notice how the DC1 axial wires depletion is reflected in the DC2 plane. This reflection moves depending on the momentum bin and would be hard to model using the traditional cuts.

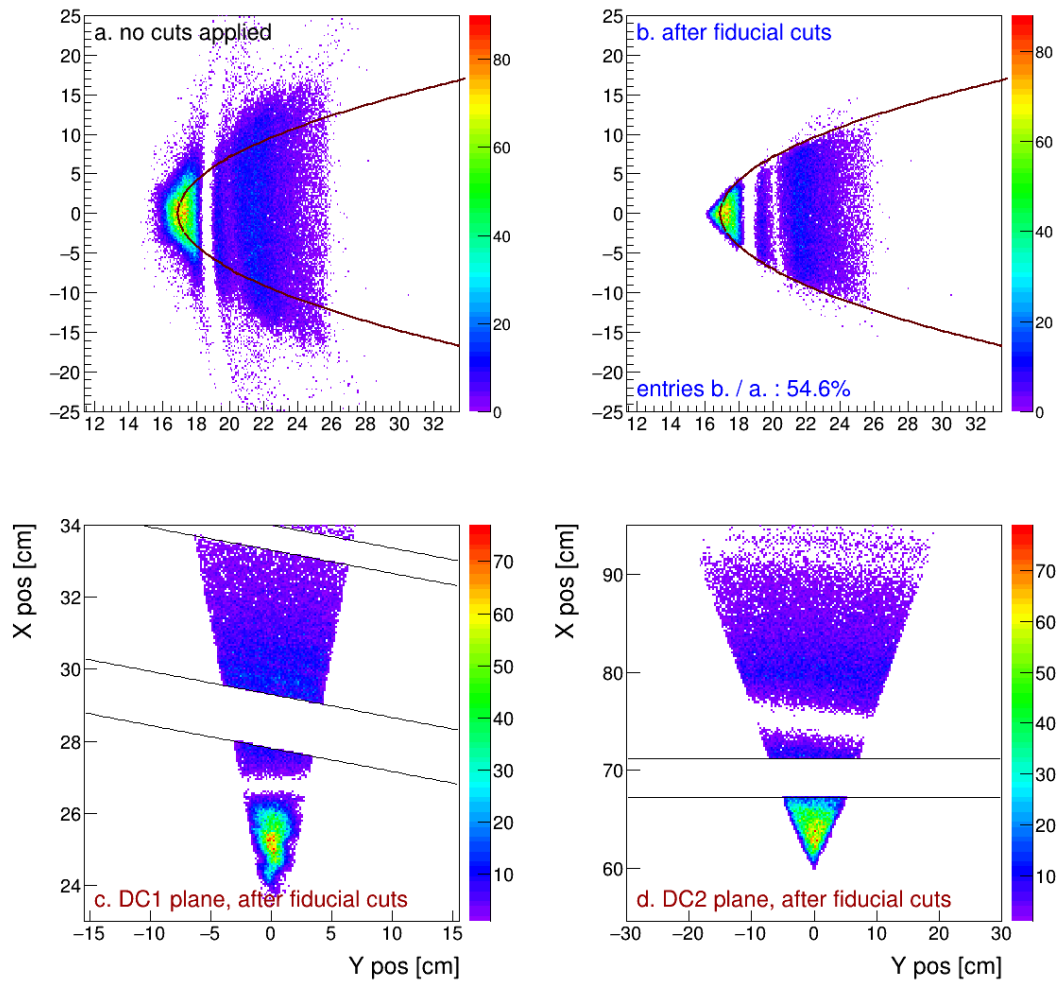
**Fiducial Cut – Sector 5 – Momentum:  $3.8 \pm 0.24$  GeV**


Figure 35:  $\phi$  vs  $\theta$  distributions in sector 5 for all the momentum bin before the XY fiducial cuts.

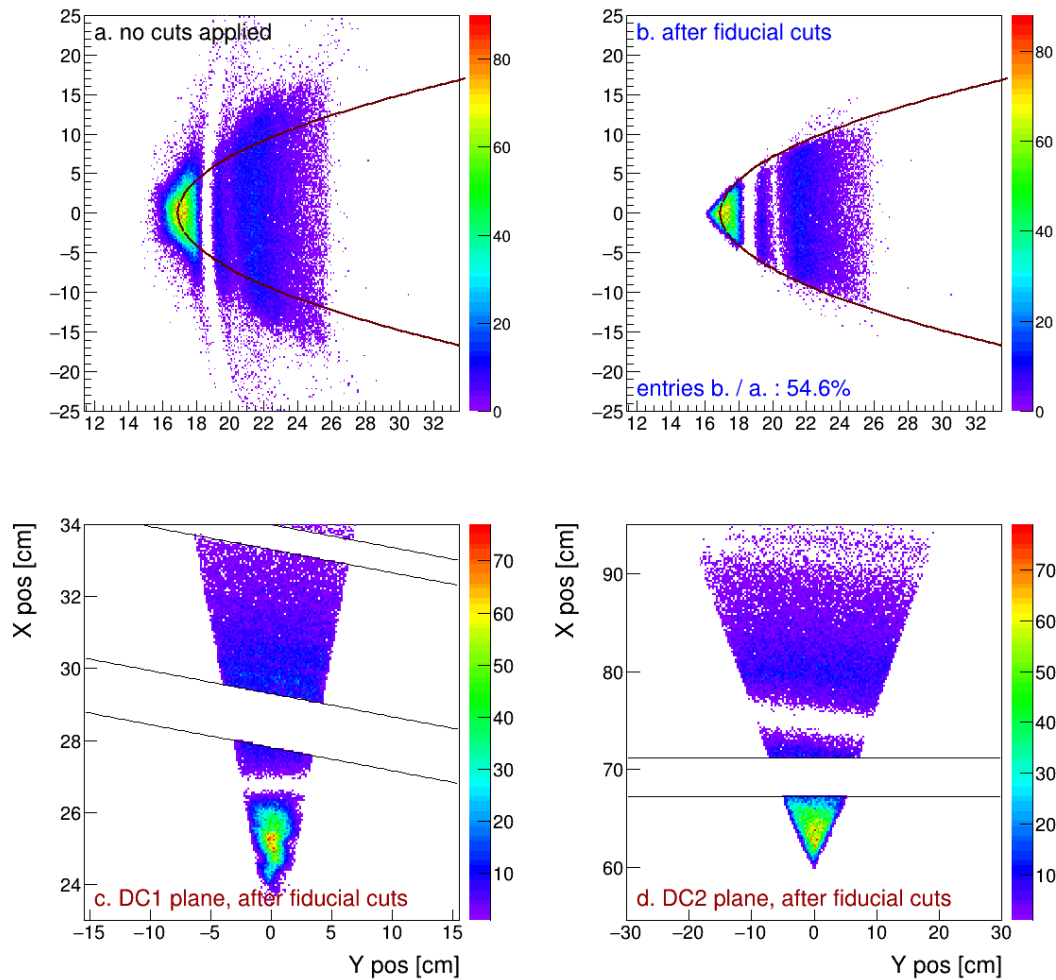
**Fiducial Cut - Sector 5 - Momentum:  $3.8 \pm 0.24$  GeV**

Figure 36:  $\phi$  vs  $\theta$  distributions in sector 5 for all the momentum bin after the XY fiducial cuts.

## 5 Electron Kinematic Correction

### 5.1 Introduction

The reconstructed momentum of the electron is slightly incorrect, due to drift chamber misalignments and an inaccurate magnetic field map. This is reflected on quantities like  $W$  or missing masses, and directly affect this analysis cuts and acceptance calculations.

Here we apply the same momentum correction extrapolated in [17]. The resulting elastic peak  $W$ , the  $eP(\pi^0)$  and  $eP(\eta)$  missing masses are improved as shown in the following sample of plots.

### 5.2 Correction effects on the elastic peak

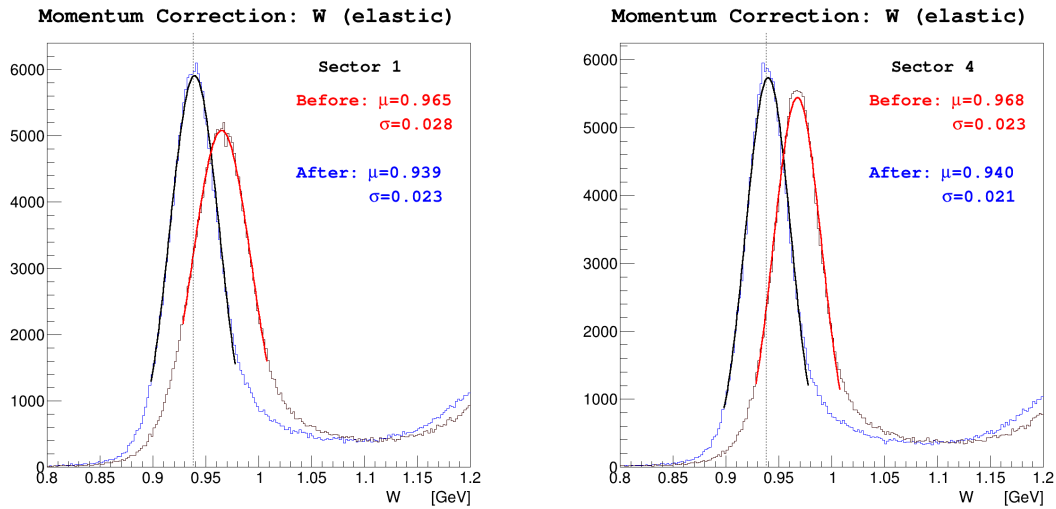


Figure 37: The  $W$  distribution before and after the correction for sector 1 (left) and sector 4 (right). The width and the position of the elastic peak are improved in all sectors.

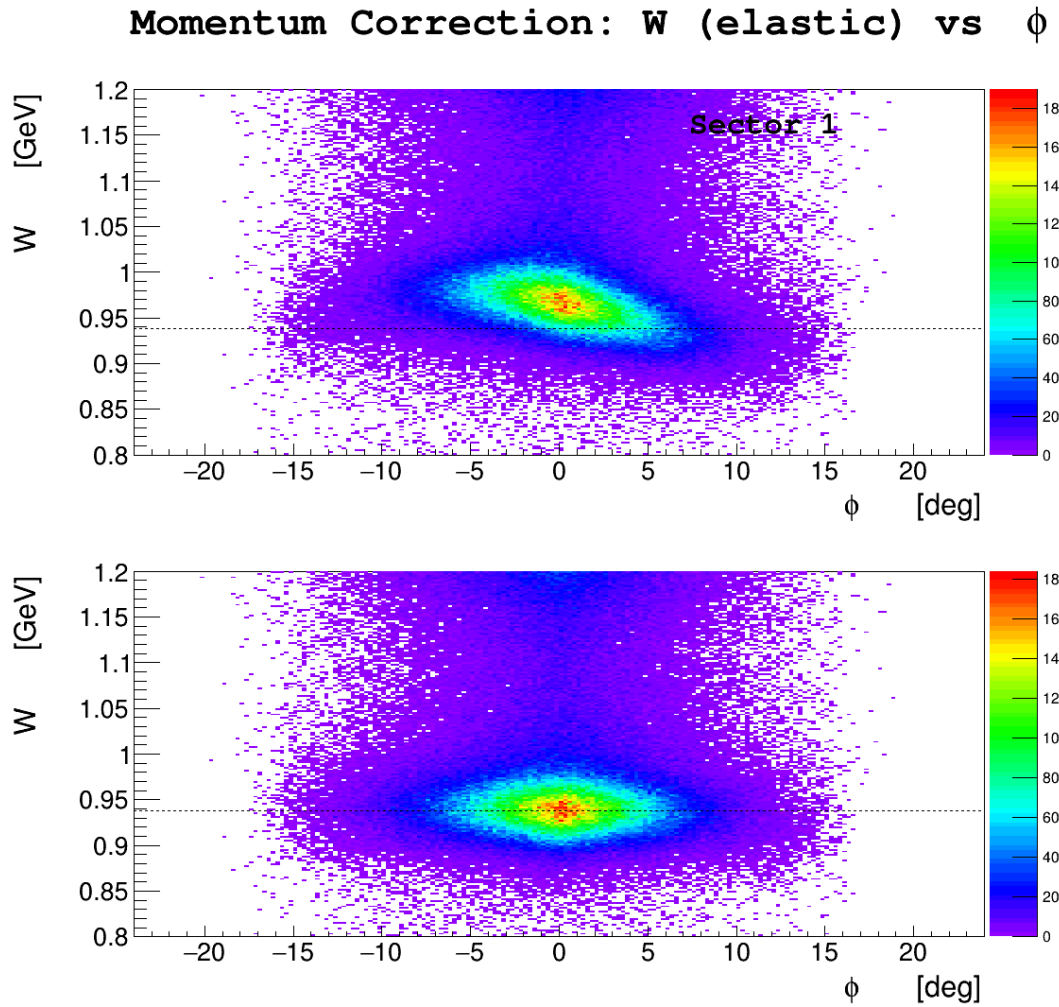


Figure 38: The  $W$  distribution as a function of  $\phi$  before (top) and after (bottom) the correction for sector 1. The distribution is flat after the correction.

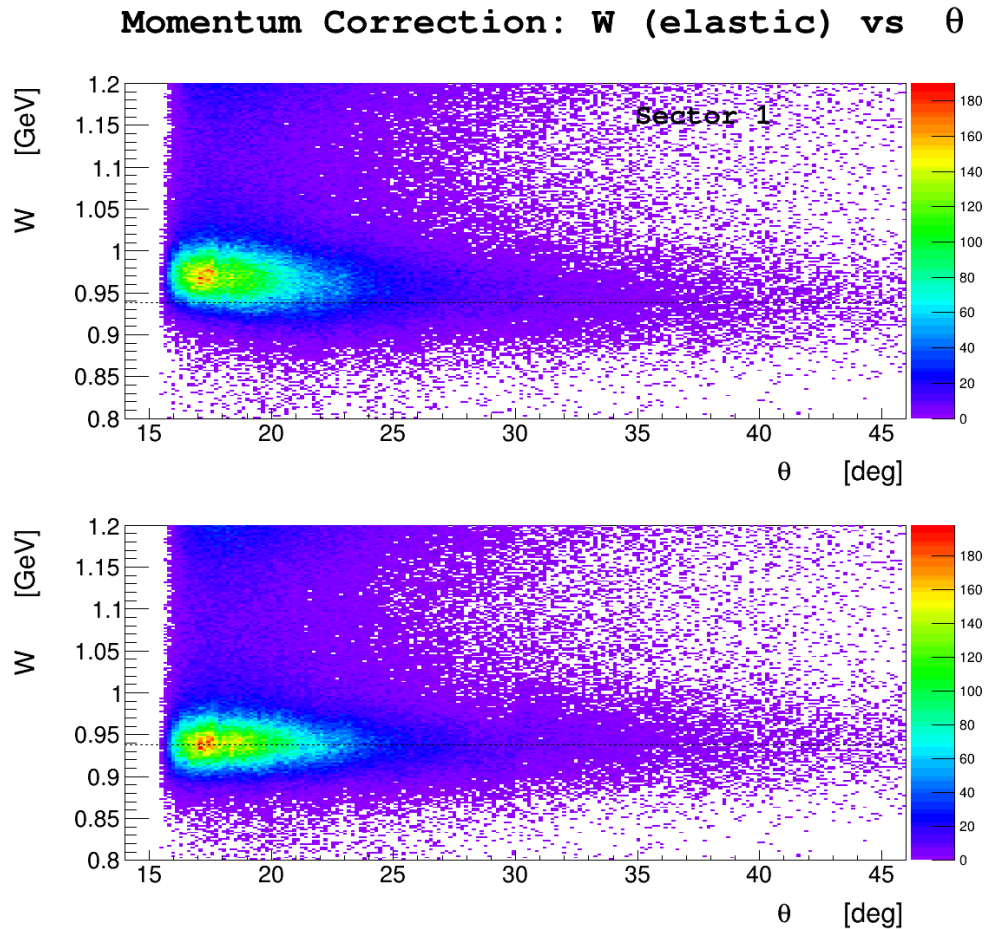


Figure 39: The  $W$  distribution as a function of  $\theta$  before (top) and after (bottom) the correction for sector 1. The distribution is flat after the correction.

### 5.3 Correction effects on the $eP(\pi^0)$ missing mass

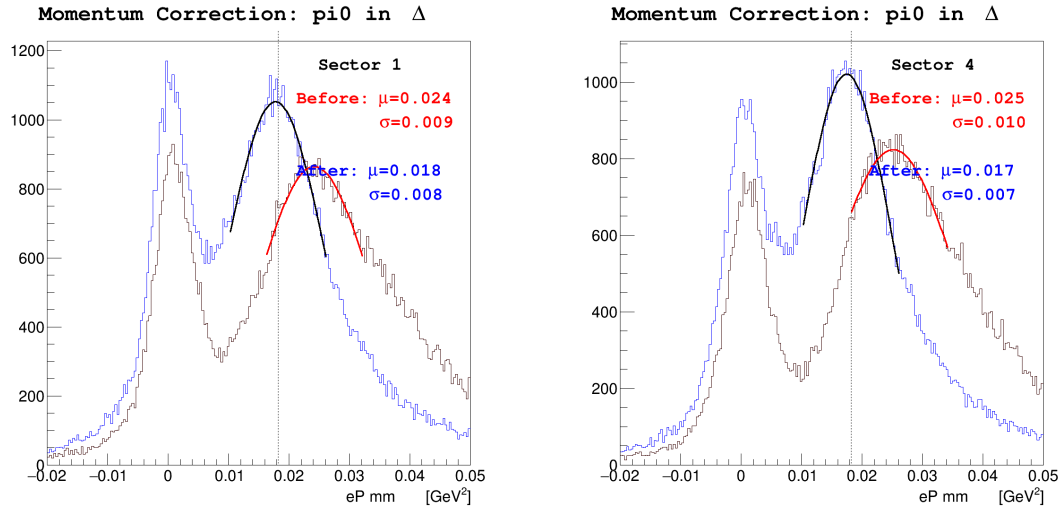


Figure 40: The  $eP(\pi^0)\ mm^2$  distribution before and after the correction for sector 1 (left) and sector 4 (right). The width and the position of the  $\pi^0$  peak are improved in all sectors.

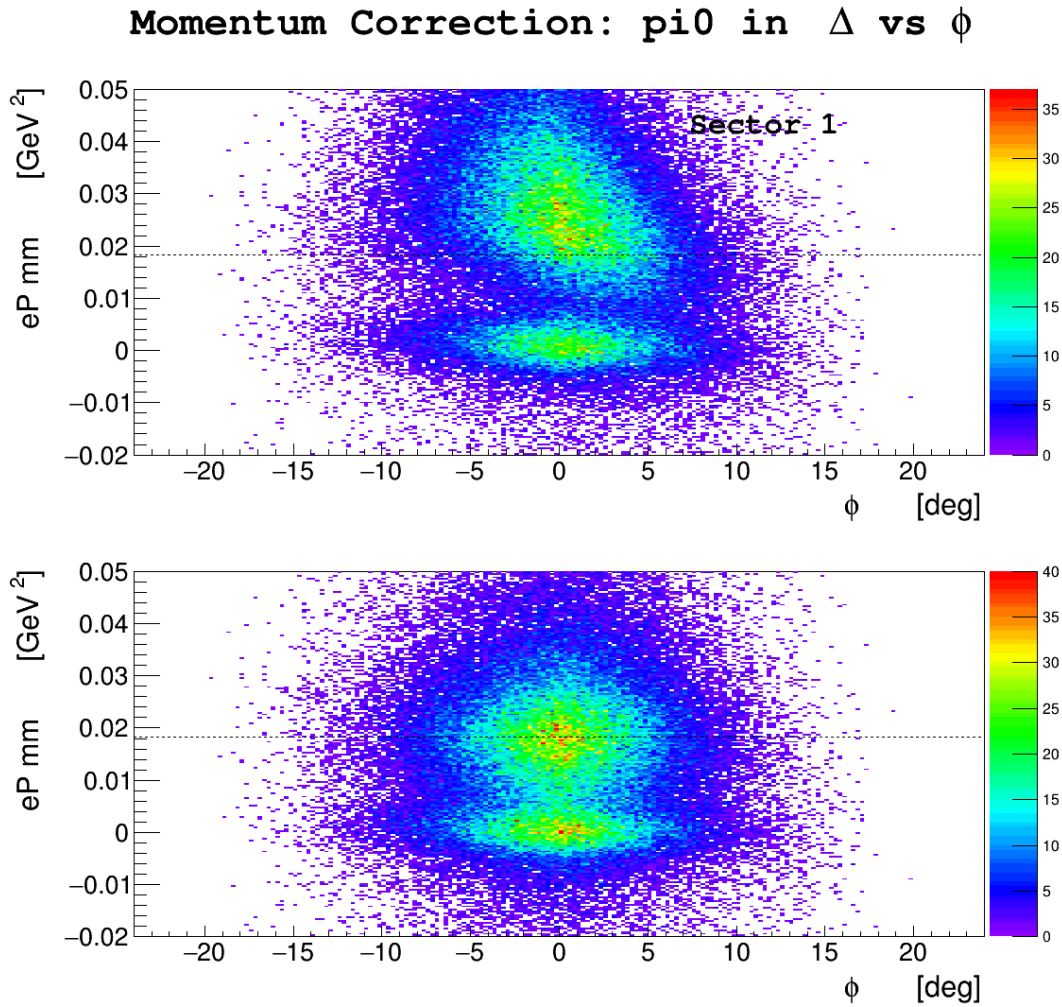


Figure 41: The  $eP(\pi^0)$   $mm^2$  distribution as a function of  $\phi$  before (top) and after (bottom) the correction for sector 1. The distribution is flat after the correction.

## 5.4 Correction effects on the $eP(\eta)$ missing mass

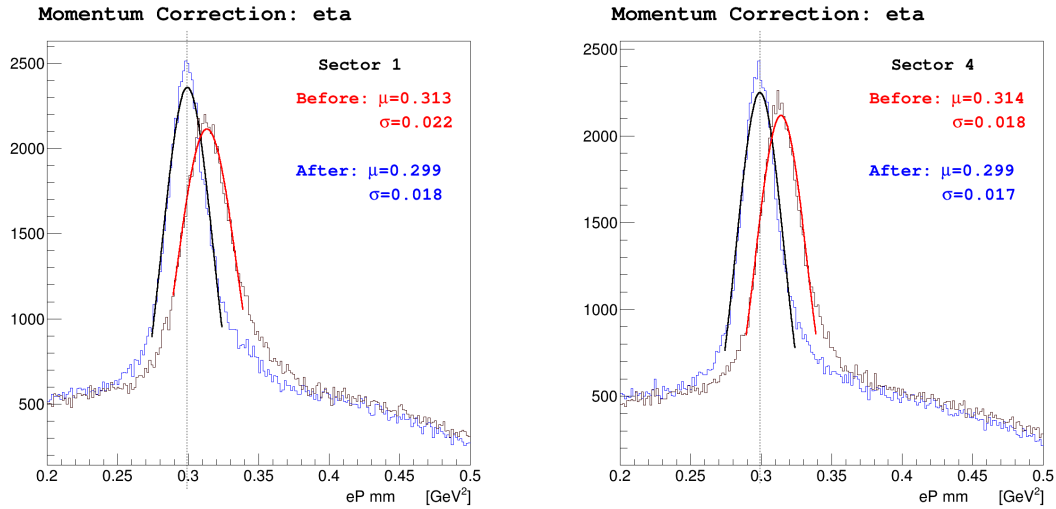


Figure 42: The  $eP(\eta) \text{ mm}^2$  distribution before and after the correction for sector 1 (left) and sector 4 (right). The width and the position of the  $\eta$  peak are improved in all sectors.

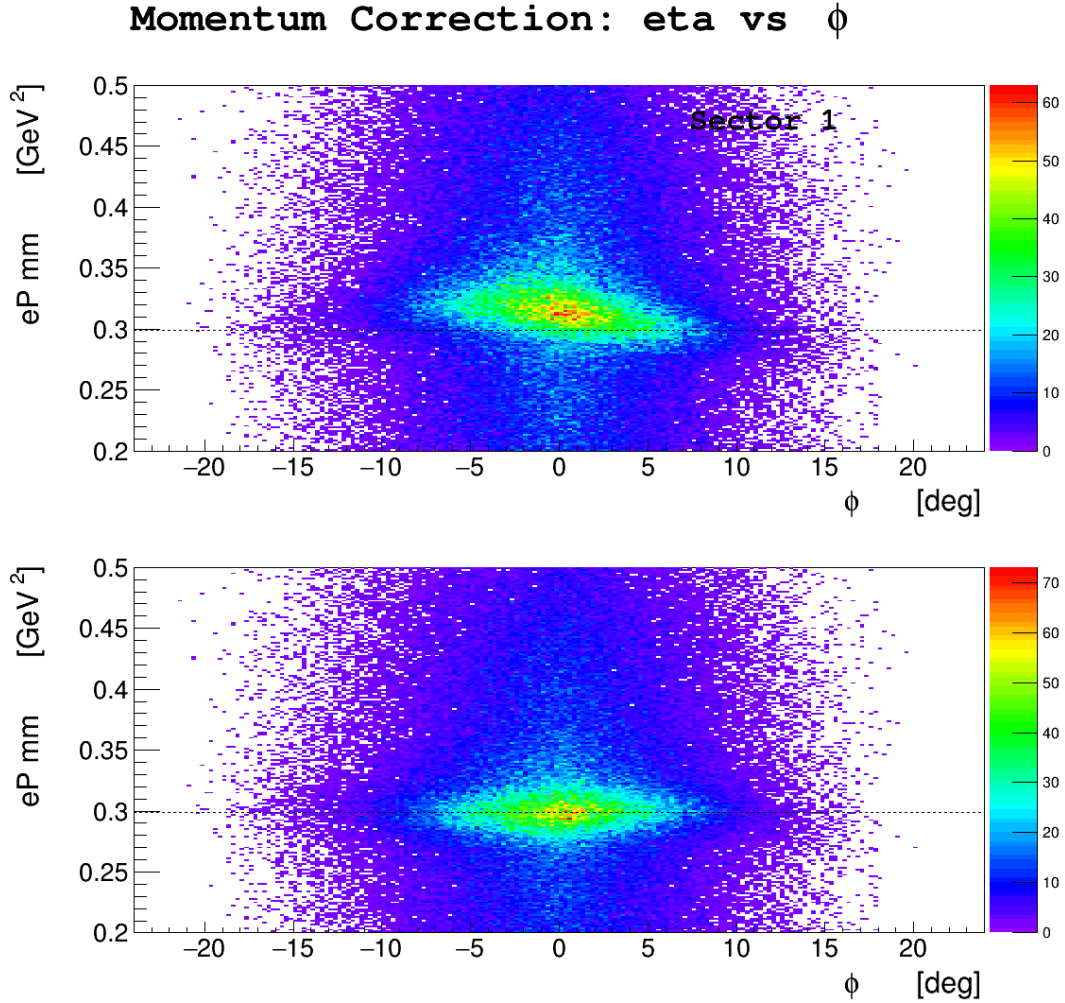


Figure 43: The  $eP(\eta) \text{ mm}^2$  distribution as a function of  $\phi$  before (top) and after (bottom) the correction for sector 1. The distribution is flat after the correction.

The complete set of plots is available at [18]. The full set of parameters and the function used in the correction is available in appendix .3.

## References

- [1] S. Stepanya, *Private Communication*
- [2] M. Osipenko, *Private Communication*
- [3] F.X. Girod, P. Khetarpal, *Private Communication*
- [4] M.D. Mestayer et al., The CLAS Drift Chamber System *Nucl. Inst. and Meth. A* 449, 81 (2000)
- [5] E.S. Smith et al., The Time-of-Flight System for CLAS, *Nucl. Inst. and Meth. A* 432, 265 (1999)
- [6] M. Amarian et al., The CLAS Forward Electromagnetic Calorimeter, *Nucl. Inst. and Meth. A* 460, 239 (2001).
- [7] G. Adams et al., The CLAS Cerenkov Detector, *Nucl. Inst. and Meth. A* 465, 414 (2001).
- [8] K.S. Egiyan, [\*CLAS NOTE 99 - 007\*](#)
- [9] M. Osipenko, A. Vlassov and and M. Taiuti [\*CLAS NOTE 04 - 020\*](#)
- [10] M.Ungaro, *Electron identification for single  $\pi^0$  elctroproduction in the first and second resonance regions*
- [11] E.S. Smith et al., The Time-of-Flight System for CLAS, *Nucl. Inst. and Meth. A* 432, 265 (1999)
- [12] B. Niczyporuk, [\*CLAS-NOTE 91 - 001\*](#)
- [13] M.Ungaro, *Proton identification for single  $\pi^0$  elctroproduction in the first and second resonance regions*
- [14] Valeri Koubarovski, *Private Communication.*
- [15] M.Ungaro, *Single  $\pi^0$  elctroproduction from  $\Delta(1232)$  at high momentum transferred with CLAS*
- [16] M.Ungaro, *Electron fiducial cut for single  $\pi^0$  elctroproduction in the first and second resonance regions*
- [17] M.Ungaro, *Single  $\pi^0$  elctroproduction from  $\Delta(1232)$  at high momentum transferred with CLAS*
- [18] M.Ungaro, *Electron Momentum Corrections for single  $\pi^0$  elctroproduction in the first and second resonance regions*

M. Ungaro, K. Joo

## .1 Fiducial cut tent function

```

double tent(double *X, double *par) {
    double x = X[0];

    double p0 = par[0];
    double p1 = par[1];
    double p2 = par[2];
    double p3 = par[3];
    double p4 = par[4];
    double a = par[5];

    // parabola parameters
    // y = ax^2 + bx + c
    // a = par[5]
    // with two constrains given by the two points at x,y = (p1, p4), (p2, p4):
    double b = -a * (p1 * p1 - p2 * p2) / (p1 - p2);
    double c = p4 - a * p1 * p1 - b * p1;

    if (x < p1 - p0) return 0;                                // no signal
    if (x >= p1 - p0 && x < p1) return (p4 / p0) * (x - p1 + p0); // steep rise
    if (x >= p1 && x < p2) return a * x * x + b * x + c;        // parabola
    if (x >= p2 && x < p2 + p3) return (p4 / p3) * (-x + p2 + p3); // steep descend
    if (x >= p2 + p3) return 0;                                // no signal

    return 0;
}

```

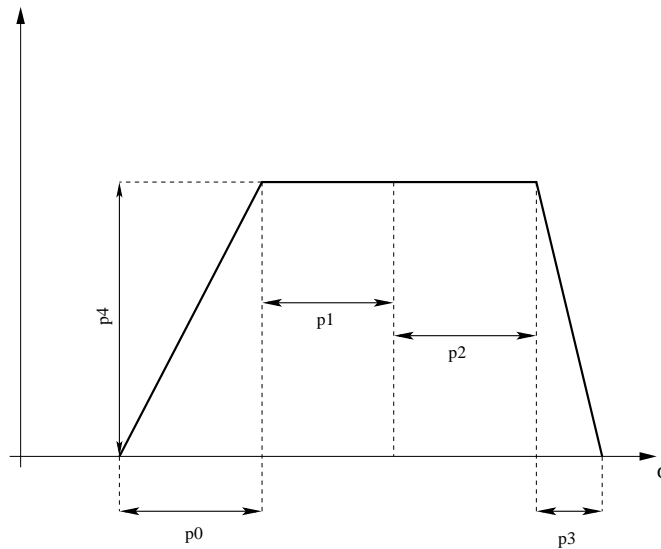


Figure 44: The trapezoid function used for the  $\phi$  fit. The parameters  $p_1$  and  $p_2$  determine the fiducial cut lower and upper limits.

The trapezoid fit gives the parameters  $p_1$  and  $p_2$  described above for each  $\theta$  considered in each momentum bin.

## .2 Fiducial cut tent function

```
double tent(double *X, double *par) {
    double x = X[0];

    double p0 = par[0];
    double p1 = par[1];
    double p2 = par[2];
    double p3 = par[3];
    double p4 = par[4];
    double a = par[5];

    // parabola parameters
    // y = ax^2 + bx + c
    // a = par[5]
    // with two constraints given by the two points at x,y = (p1, p4), (p2, p4):
    double b = -a * (p1 * p1 - p2 * p2) / (p1 - p2);
    double c = p4 - a * p1 * p1 - b * p1;

    if (x < p1 - p0) return 0;                                // no signal
    if (x >= p1 - p0 && x < p1) return (p4 / p0) * (x - p1 + p0); // steep rise
    if (x >= p1 && x < p2) return a * x * x + b * x + c;        // parabola
    if (x >= p2 && x < p2 + p3) return (p4 / p3) * (-x + p2 + p3); // steep descend
    if (x >= p2 + p3) return 0;                                // no signal

    return 0;
}
```

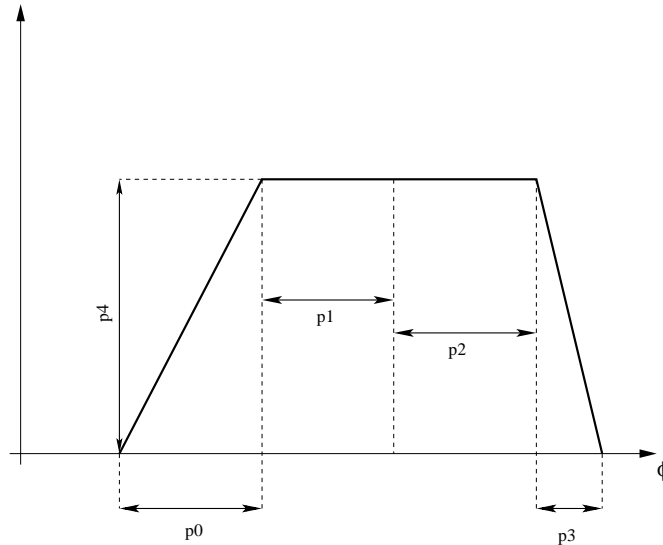


Figure 45: The trapezoid function used for the  $\phi$  fit. The parameters  $p_1$  and  $p_2$  determine the fiducial cut lower and upper limits.

The trapezoid fit gives the parameters  $p_1$  and  $p_2$  described above for each  $\theta$  considered in each momentum bin.

### **.3 Momentum Correction Parameters and function**

Below are the parameters used to correct the electron momentum.

Sector 1:

```
a: 4.68752 -1.85247 0.309905 -0.0287839 0.00164415
    -6.01897e-05 1.41784e-06 -2.07918e-08 1.72727e-10 -6.20909e-13
b: -0.141375 0.0658297 -0.0124197 0.00125396 -7.61444e-05
    2.9224e-06 -7.15019e-08 1.08187e-09 -9.22762e-12 3.39275e-14
c: 0.325959 -0.104809 0.0146168 -0.00116222 5.81367e-05
    -1.89952e-06 4.05847e-08 -5.47376e-10 4.23328e-12 -1.43176e-14
d: -0.011592 0.00376657 -0.000525382 4.14727e-05 -2.04875e-06
    6.58696e-08 -1.38172e-09 1.82743e-11 -1.38541e-13 4.59477e-16
```

The function used to correct the electron momentum is:

```
V4 mom_corr::m_corr(V4 x) {
    if (x.theta() / degree < 14 || x.theta() / degree > 30) return x;

    V4 y;
    double corr;
    double a, b, c, d;
    double theta = x.theta() / degree;
    double phi = loc_phi(x) / degree;
    int s = sector(x) - 1;

    a = b = c = d = 0;

    for (int p = 0; p < 10; p++) a = a + par_par_phi[s][0][p] * pow(theta, p);
    for (int p = 0; p < 10; p++) b = b + par_par_phi[s][1][p] * pow(theta, p);
    for (int p = 0; p < 10; p++) c = c + par_par_phi[s][2][p] * pow(theta, p);
    for (int p = 0; p < 10; p++) d = d + par_par_phi[s][3][p] * pow(theta, p);

    corr = (a + b * phi + c * phi * phi + d * phi * phi * phi) * GeV;

    y.x = (x.mod() + corr) * sin(x.theta()) * cos(x.phi());
    y.y = (x.mod() + corr) * sin(x.theta()) * sin(x.phi());
    y.z = (x.mod() + corr) * cos(x.theta());
    y.t = sqrt(y.mod() * y.mod() + electron_mass * electron_mass);

    return y;
}
```